

Discovery and Follow-up of ASASSN-19dj: An X-ray and UV Luminous TDE in an Extreme Post-Starburst Galaxy

Jason T. Hinkle¹★, T. W.-S. Holoien²†, K. Auchettl^{15,16,3,4}, B. J. Shappee¹, J. M. M. Neustadt⁵, A. V. Payne¹‡, J. S. Brown⁴, C. S. Kochanek^{5,6}, K. Z. Stanek^{5,6}, M. J. Graham⁷, M. A. Tucker¹§, A. Do¹, J. P. Anderson⁸, S. Bose^{5,6}, P. Chen⁹, D. A. Coulter⁴, G. Dimitriadis⁴, Subo Dong⁹, R. J. Foley⁴, M. E. Huber¹, T. Hung⁴, C. D. Kilpatrick⁴, G. Pignata^{11,10}, J. L. Prieto^{12,10}, C. Rojas-Bravo⁴, M. R. Siebert⁴, B. Stalder¹³, Todd A. Thompson^{5,6}, J. L. Tonry¹, P. J. Vallely⁵, & J. P. Wisniewski¹⁴

¹*Institute for Astronomy, University of Hawai'i, 2680 Woodlawn Dr., Honolulu, HI 96822, USA*

²*The Observatories of the Carnegie Institution for Science, 813 Santa Barbara St., Pasadena, CA 91101, USA*

³*DARK, Niels Bohr Institute, University of Copenhagen, Lyngbyvej 2, 2100 Copenhagen, Denmark*

⁴*Department of Astronomy and Astrophysics, University of California, Santa Cruz, CA 95064, USA*

⁵*Department of Astronomy, The Ohio State University, 140 West 18th Avenue, Columbus, OH 43210, USA*

⁶*Center for Cosmology and Astroparticle Physics, The Ohio State University, 191 W. Woodruff Avenue, Columbus, OH 43210, USA*

⁷*California Institute of Technology, 1200 E. California Blvd, Pasadena, CA 91125, USA*

⁸*European Southern Observatory, Alonso de Córdova 3107, Vitacura, Casilla 19001, Santiago, Chile*

⁹*Kavli Institute for Astronomy and Astrophysics, Peking University, Yi He Yuan Road 5, Hai Dian District, Beijing 100871, China*

¹⁰*Millennium Institute of Astrophysics, Santiago, Chile*

¹¹*Departamento de Ciencias Físicas, Universidad Andres Bello, Avda. Republica 252, Santiago, Chile*

¹²*Núcleo de Astronomía de la Facultad de Ingeniería y Ciencias, Universidad Diego Portales, Av. Ejército 441, Santiago, Chile*

¹³*Rubin Observatory Project Office, 950 North Cherry Avenue, Tucson, AZ 85719, USA*

¹⁴*Homer L. Dodge Department of Physics & Astronomy, The University of Oklahoma, 440 W. Brooks Street, Norman, OK 73019, USA*

¹⁵*School of Physics, The University of Melbourne, Parkville, VIC 3010, Australia*

¹⁶*ARC Centre of Excellence for All Sky Astrophysics in 3 Dimensions (ASTRO 3D), Australia*

22 December 2024

ABSTRACT

We present observations of ASASSN-19dj, a nearby tidal disruption event (TDE) discovered in the post-starburst galaxy KUG 0810+227 by the All-Sky Automated Survey for Supernovae (ASAS-SN) at a distance of $d \simeq 98$ Mpc. We observed ASASSN-19dj from -21 to 392 days relative to peak UV/optical emission using high-cadence, multi-wavelength spectroscopy and photometry. From the ASAS-SN g -band data, we determine that the TDE began to brighten on 2019 February 6.8 and for the first 25 days the rise was consistent with a flux $\propto t^2$ power-law. ASASSN-19dj peaked in the UV/optical on 2019 March 6.5 (MJD = 58548.5) at a bolometric luminosity of $L = (6.2 \pm 0.2) \times 10^{44}$ erg s⁻¹. Initially remaining roughly constant in X-rays and slowly fading in the UV/optical, the X-ray flux increased by over an order of magnitude ~ 225 days after peak, resulting from the expansion of the X-ray emitting surface. The late-time X-ray emission is well-fit by a blackbody with an effective radius of $\sim 1 \times 10^{12}$ cm and a temperature of $\sim 6 \times 10^5$ K. Analysis of Catalina Real-Time Transient Survey images reveals a nuclear outburst roughly 14.5 years earlier with a smooth decline and a luminosity of $L_V \geq 1.4 \times 10^{43}$ erg s⁻¹, although the nature of the flare is unknown. ASASSN-19dj occurred in the most extreme post-starburst galaxy yet to host a TDE, with Lick $H\delta_A = 7.67 \pm 0.17$ Å.

Key words: accretion, accretion discs — black hole physics — galaxies: nuclei

★ E-mail: jhinkle6@hawaii.edu

† Carnegie Fellow

1 INTRODUCTION

Supermassive black holes (SMBHs) are known to reside in the centers of most massive galaxies (e.g., Kormendy & Richstone 1995; Magorrian et al. 1998; Rees 1988; Ho 2008; Gültekin et al. 2009; Kormendy & Ho 2013). If mass is actively accreting onto these SMBHs, they can be detected as Active Galactic Nuclei (AGN). Conversely, direct detections of inactive SMBHs are difficult, mainly limited to our own black hole (Sgr A*; Ghez et al. 2005), or massive ($\gtrsim 10^6 M_\odot$) SMBHs in nearby ($\lesssim 50$ Mpc) galaxies, where stars (e.g., Kormendy et al. 1996; Gebhardt et al. 2011) and/or gas (e.g., Ford et al. 1994; Atkinson et al. 2005) within the SMBH's sphere of influence can be resolved. Only one SMBH, Pöwehi in M87, has been directly observed, by the Event Horizon Telescope (Event Horizon Telescope Collaboration et al. 2019). Tidal disruption events (TDEs) provide an opportunity to study otherwise inactive SMBHs at greater distances.

A TDE occurs when a star passes within the tidal radius of a SMBH and is torn apart, resulting in a luminous accretion flare (Rees 1988; Phinney 1989; Evans & Kochanek 1989; Ulmer 1999; Komossa 2015; Stone et al. 2019). Early theoretical work predicted that the blackbody temperatures of TDEs should be on the order of 10^5 K, consistent with a peak in the soft X-ray band (e.g., Lacy et al. 1982; Rees 1988; Evans & Kochanek 1989; Phinney 1989), but observational studies have discovered a breadth of TDE phenomenology. For example, TDE candidates have been detected in the hard X-ray (e.g., Bloom et al. 2011; Burrows et al. 2011; Cenko et al. 2012b; Pasham et al. 2015), soft X-ray (e.g., Bade et al. 1996; Komossa & Bade 1999; Komossa & Greiner 1999; Grupe et al. 1999; Auchettl et al. 2017), ultraviolet (UV) (e.g., Stern et al. 2004; Gezari et al. 2006, 2008, 2009), and optical (e.g., van Velzen et al. 2011; Gezari et al. 2012; Cenko et al. 2012a; Arcavi et al. 2014; Chornock et al. 2014; Holoien et al. 2014b; Vinkó et al. 2015; Holoien et al. 2016b,c; Brown et al. 2018; Holoien et al. 2019a,b), with many showing emission in multiple energy bands. The diversity seen in these events fueled a broad range of theoretical investigations (e.g., Lodato et al. 2015; Krolik et al. 2016; Svirski et al. 2017; Ryu et al. 2020; Krolik et al. 2020). The unifying model of Dai et al. (2018) may provide an explanation of the diversity, positing that many of the observed multi-wavelength photometric and spectroscopic properties of TDEs are a result of the viewing angle. Despite this, the origin of the UV/optical emission is still debated (e.g., Jiang et al. 2016; Bonnerot et al. 2017; Lu & Bonnerot 2020).

Observations of TDEs may provide information on the physics of accretion (e.g., Lodato & Rossi 2011; Guillochon & Ramirez-Ruiz 2015; Metzger & Stone 2016; Shiokawa et al. 2015), shock physics (e.g., Lodato et al. 2009), jet formation (e.g., Farrar & Piran 2014; Wang & Liu 2016; Biehl et al. 2018), and the environment and growth of SMBHs (e.g., Auchettl et al. 2018). However, the characteristics of the observed emission from TDEs, such as their light curves, spectroscopic evolution (both optical and X-ray), blackbody properties, etc., are a function of many physical parameters. Such properties include the star's impact parameter (e.g.,

Guillochon & Ramirez-Ruiz 2013, 2015; Gafton & Rosswog 2019), mass (e.g., Gallegos-Garcia et al. 2018; Mockler et al. 2019; Law-Smith et al. 2019), composition (e.g., Kochanek 2016a), evolutionary stage (e.g., MacLeod et al. 2012), age (e.g., Gallegos-Garcia et al. 2018), and spin (e.g., Golightly et al. 2019). Additionally, stellar demographics (e.g., Kochanek 2016b), the fraction of accreted stellar material (e.g., Metzger & Stone 2016; Coughlin & Nixon 2019), and the geometry of accretion (e.g., Kochanek 1994; Lodato & Rossi 2011; Guillochon & Ramirez-Ruiz 2015; Metzger & Stone 2016; Dai et al. 2015; Shiokawa et al. 2015; Dai et al. 2018) may affect the observed emission.

It has also been shown that TDE emission may be sensitive to black hole spin and mass (e.g., Ulmer 1999; Graham et al. 2001; Mockler et al. 2019; Gafton & Rosswog 2019), making TDEs useful probes of otherwise quiescent SMBHs. As such, TDE light curves can be used to constrain the masses of SMBHs, which are consistent with those derived from other methods (Mockler et al. 2019). While there are a large number of potentially relevant physical parameters, the observed UV/optical emission is relatively well fit by a blackbody (e.g., Gezari et al. 2012; Holoien et al. 2014a, 2016b,c; Brown et al. 2016; Hung et al. 2017; Holoien et al. 2018, 2019b; Leloudas et al. 2019; van Velzen et al. 2020; Holoien et al. 2020). It has also been shown that the peak UV/optical luminosities of TDEs are related to their decline rates (Mockler et al. 2019; Hinkle et al. 2020), with more luminous TDEs declining more slowly after peak. As the number of TDEs increases, they will provide a more complete picture of SMBH growth and evolution via accretion and the central environments of galaxies.

The spectroscopic properties of optical TDEs are varied (e.g., Arcavi et al. 2014; Hung et al. 2017; Leloudas et al. 2019; Wevers et al. 2019b; van Velzen et al. 2020; Holoien et al. 2020), with differences in observed species, line strengths/widths, and line ratios. Possible explanations for this variety are details in the physics of photoionization (e.g., Guillochon et al. 2014; Gaskell & Rojas Lobos 2014; Roth et al. 2016; Kara et al. 2018a; Leloudas et al. 2019), differences in the composition of stars due to evolution (Kochanek 2016a), the viewing geometry with respect to an accretion disk (e.g., Holoien et al. 2019a; Short et al. 2020; Hung et al. 2020), or even the disruption of helium stars (Gezari et al. 2012; Strubbe & Murray 2015). Additionally, there have been variations in the times at which strong emission lines appear (e.g., Holoien et al. 2019a,b, 2020). An even larger sample of optically-bright TDEs will better constrain the mechanisms that influence the observed emission from such events.

TDEs are rare, with an expected frequency between 10^{-4} and 10^{-5} yr $^{-1}$ per galaxy (e.g., van Velzen & Farrar 2014; Holoien et al. 2016b; van Velzen 2018; Auchettl et al. 2018). Interestingly though, TDEs seem to prefer post-starburst host galaxies. In such galaxies, the TDE rates can be enhanced by up to 200 times as compared to the average rates (e.g., Arcavi et al. 2014; French et al. 2016; Law-Smith et al. 2017; Graur et al. 2018). Combining these suggests that in the most extreme post-starbursts, TDEs can occur at roughly the same rate as other bright transients like supernovae.

There are few observations of the early-time evolution of TDEs, a time period that may be important to understand

‡ NASA Fellowship Activity Fellow

§ DOE CSGF Fellow

ing how the disrupted stellar material settles into an accretion flow. With the advent of transient surveys like the All-Sky Automated Survey for Supernovae (ASAS-SN; Shappee et al. 2014; Kochanek et al. 2017), the Asteroid Terrestrial Impact Last Alert System (ATLAS; Tonry et al. 2018), the Zwicky Transient Facility (ZTF; Bellm et al. 2019), the Panoramic Survey Telescope and Rapid Response System (Pan-STARRS; Chambers et al. 2016) and the Young Supernova Experiment (YSE; Jones et al. 2019), many more TDEs are being discovered. This includes an increasing number of TDEs discovered before their peak brightness (e.g., Holoien et al. 2019a,b; Leloudas et al. 2019; van Velzen et al. 2019; Wevers et al. 2019b; van Velzen et al. 2020; Holoien et al. 2020).

While these fast-cadence, wide-field optical surveys are ideal for discovering TDEs, a significant fraction of emission from some events is in the soft X-ray band (e.g., Ulmer 1999; Auchettl et al. 2017). Recently, an increasing number of TDE candidates discovered in the optical have exhibited strong X-ray emission. Examples include ASASSN-14li (e.g., Miller et al. 2015; Holoien et al. 2016b; Brown et al. 2017), ASASSN-15oi (e.g., Holoien et al. 2016a; Gezari et al. 2017; Holoien et al. 2018), ASASSN-18ul (Wevers et al. 2019b, ; Payne et al., in preparation), Gaia19bpt (van Velzen et al. 2020), ZTF19aapreis (van Velzen et al. 2020), and the TDE studied in this work, ASASSN-19dj. The combination of UV, optical and X-ray has given greater insight on the formation of an accretion disk, reprocessing, and the differences between thermal (non-jetted) and non-thermal (jetted) TDEs (e.g., Auchettl et al. 2017). In general, long-term X-ray light curves of TDE candidates are required to distinguish them from AGN and to study detailed accretion physics (e.g., Auchettl et al. 2018).

In this paper we present the discovery and observations of ASASSN-19dj. Smaller datasets on ASASSN-19dj have been analysed by Liu et al. (2019) and as part of the larger sample in van Velzen et al. (2020). Here we provide analysis of the host galaxy in addition to a longer observational baseline with corresponding detailed analysis of the UV/optical photometric, optical spectroscopic, and X-ray properties of ASASSN-19dj. Throughout the paper we assume a cosmology of $H_0 = 69.6 \text{ km s}^{-1} \text{ Mpc}^{-1}$, $\Omega_M = 0.29$, and $\Omega_\Lambda = 0.71$. This paper is organised as follows. In Section 2 we detail the discovery and observations of the TDE. In Section 3 we present the analysis of our results. Finally, our analysis is summarized in Section 4.

2 DISCOVERY AND OBSERVATIONS

ASASSN-19dj (α, δ) = (08:13:16.96, +22:38:54.00) was discovered in the g -band in data from the ASAS-SN “Bohdan Paczyński” unit in Cerro Tololo, Chile on 2019 February 22 (Brimacombe et al. 2019). Its discovery was announced on the Transient Name Server (TNS), and assigned the name AT 2019azh¹. Rather than anonymise the discovering survey, in this paper, we will continue to refer to the TDE by its survey name ASASSN-19dj. ASASSN-19dj is located in the nucleus of the post-starburst galaxy KUG 0810+227, at

a redshift of $z = 0.022346$ (Adelman-McCarthy et al. 2006). This redshift corresponds to a luminosity distance of 97.9 Mpc, making ASASSN-19dj one of the closest TDEs discovered to date. The g -band reference used for host subtraction, the discovery image of ASASSN-19dj, and a false-colour Pan-STARRS gri image of the host galaxy² (Chambers et al. 2016) are shown in Figure 1. The circle marking the location of ASASSN-19dj is $15''0$ in radius, the same as the apertures used for the photometry presented in this paper.

Multiple spectroscopic observations were obtained shortly after discovery. Both the Nordic Optical Telescope Unbiased Transient Survey (NUTS; Heikkilä et al. 2019) and the extended Public ESO Spectroscopic Survey for Transient Objects (ePESSTO; Barbarino et al. 2019) obtained spectra that showed a strong blue continuum with few strong spectral features compared to the Sloan Digital Sky Survey (SDSS; York et al. 2000) host spectrum (see §2.1). The strong blue continuum, the appearance of broad $H\alpha$ emission lines, and a position consistent with the nucleus of the host galaxy made ASASSN-19dj a strong TDE candidate. Based on this, we triggered spectroscopic and ground-based photometric (Swope and LCOGT) follow-up of ASASSN-19dj.

Using ZTF and Neil Gehrels Swift Gamma-ray Burst Mission (Swift; Gehrels et al. 2004) observations, van Velzen et al. (2019) observed a plateau in the optical and UV light curve between 2019 February 24.25 and 2019 March 11.45. From fits to the ZTF and Swift photometry, they found that the transient spectral energy distribution (SED) was consistent with a $T = (3.2 \pm 0.7) \times 10^4 \text{ K}$ blackbody, and measured a spatial separation from the host nucleus of $0''.07 \pm 0''.31$. They classified the source as a TDE based on the observations of multiple blue spectra, a hot blackbody temperature, position in the center of the host galaxy, and the lack of spectral features usually associated with AGN or supernovae. Using the central galaxy velocity dispersion from SDSS DR14 and the scaling relationship of Gültekin et al. (2009), they calculated a SMBH mass of $M_{BH} \lesssim 4 \times 10^6 M_\odot$, and suggested that the observed plateau in the light curve was the result of Eddington-limited accretion.

2.1 Archival Data of KUG 0810+227

KUG 0810+227 has been observed by several sky surveys across the electromagnetic spectrum. We obtained $ugriz$ and JHK_s images from SDSS Data Release 15 (Aguado et al. 2019) and the Two Micron All-Sky Survey (2MASS; Skrutskie et al. 2006), respectively. We measured aperture magnitudes using a $15''0$ aperture radius in order to capture all of the galaxy light, and used several stars in the field to calibrate the magnitudes. We also obtained an archival NUV magnitude from the Galaxy Evolution Explorer (GALEX; Martin et al. 2005) All-sky Imaging Survey (AIS) catalog and $W1$ and $W2$ magnitudes from the Wide-field Infrared Survey Explorer (WISE; Wright et al. 2010) AllWISE catalog, giving us coverage from ultraviolet through mid-infrared wavelengths.

In order to constrain the possibility of the host galaxy being an AGN, we analysed a range of archival data for KUG

¹ <https://wis-tns.weizmann.ac.il/object/2019azh>

² <http://ps1images.stsci.edu/cgi-bin/ps1cutouts?pos=123.320605325%2B22.648343&filter=color>

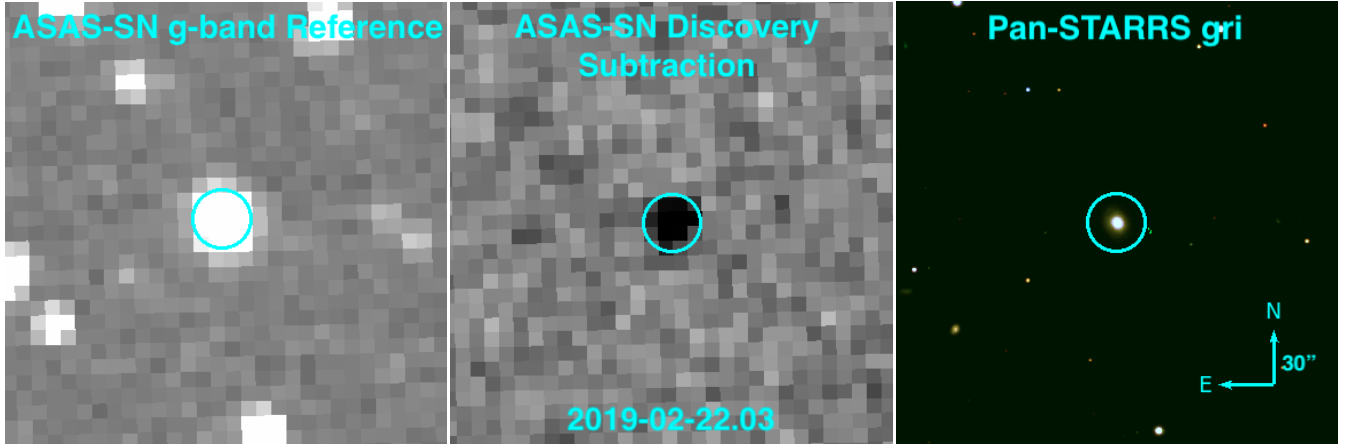


Figure 1. The ASAS-SN *g*-band reference image for the location of ASASSN19dj (left), the subtracted ASAS-SN *g*-band discovery image from 2019-02-22.03 showing flux from ASASSN19dj (center), and a combined Pan-STARRS *gri* colour image of the host galaxy (right). The cyan circle (of radius $15''0$) marks the location of ASASSN19dj.

Table 1. Archival Host Galaxy Photometry

| Filter | Magnitude | Magnitude Uncertainty |
|----------------------|-----------|-----------------------|
| <i>NUV</i> | 18.71 | 0.05 |
| <i>u</i> | 16.80 | 0.10 |
| <i>g</i> | 15.12 | 0.04 |
| <i>r</i> | 14.59 | 0.03 |
| <i>i</i> | 14.35 | 0.03 |
| <i>z</i> | 14.13 | 0.03 |
| <i>J</i> | 13.94 | 0.04 |
| <i>H</i> | 13.99 | 0.09 |
| <i>K_S</i> | 14.34 | 0.05 |
| <i>W1</i> | 15.07 | 0.03 |
| <i>W2</i> | 15.70 | 0.03 |

Archival magnitudes of the host galaxy KUG 0810+227. *ugriz* and *JHK_S* magnitudes are $15''0$ aperture magnitudes measured from SDSS and 2MASS images, respectively. The *NUV* magnitude is taken from the GALEX AIS and the *W1* and *W2* magnitudes are taken from the WISE AllWISE catalog. All magnitudes are presented in the AB system.

0810+227. Using ROSAT All-Sky Survey (RASS) data, we find no emission from the host galaxy at a 3σ upper-limit of 3.4×10^{-2} counts s^{-1} . Assuming an AGN with a photon index of $\Gamma = 1.75$ (Ricci et al. 2017) and a Galactic column density of $N_H = 4.16 \times 10^{20}$ cm^{-2} along the line of sight (HI4PI Collaboration et al. 2016), this corresponds to an unabsorbed flux of 1.2×10^{-12} erg cm^{-2} s^{-1} in the 0.3 - 10 keV band. At the distance of KUG 0810+227, this yields an X-ray luminosity of 1.4×10^{42} erg s^{-1} . This limit rules out strong AGN activity, but does not rule out the presence of a weak or low luminosity AGN (LLAGN; Tozzi et al. 2006; Marchesi et al. 2016; Liu et al. 2017; Ricci et al. 2017). The mid-infrared (MIR) colour of the host ($W1 - W2$) = 0.62 ± 0.04 mag again suggests that KUG 0810+227 does not harbour a strong AGN (e.g., Assef et al. 2013), but still does not rule out the presence of a LLAGN where the host light dominates over light from the AGN. When fitting a flat line to the WISE *W1* and *W2* light curves, we obtain reduced

χ^2 values of 2.1 and 3.0 respectively, indicating a low level of variability consistent with a LLAGN.

We fit stellar population synthesis models to the archival photometry of KUG 0810+227 (shown in Table 1) using the Fitting and Assessment of Synthetic Templates (FAST; Kriek et al. 2009) to obtain an SED of the host. Our fit assumes a Cardelli et al. (1988) extinction law with $R_V = 3.1$ and Galactic extinction of $A_V = 0.122$ mag (Schlafly & Finkbeiner 2011), a Salpeter IMF (Salpeter 1955), an exponentially declining star-formation rate, and the Bruzual & Charlot (2003) stellar population models. Based on the FAST fit, KUG 0810+227 has a stellar mass of $M_* = 9.3^{+3.0}_{-1.2} \times 10^9$ M_\odot , an age of $1.4^{+0.6}_{-0.5}$ Gyr, and an upper limit on the star formation rate of $SFR \leq 6.9 \times 10^{-2}$ M_\odot yr^{-1} . The best fit age is slightly higher than the stellar ages of other TDE host galaxies (~ 0.5 Gyr French et al. 2017). Using the sample of Mendel et al. (2014) to compute a scaling relation between stellar mass and bulge mass, we estimate a bulge mass of $\sim 10^{9.7}$ M_\odot . We then use the $M_B - M_{BH}$ relation of McConnell & Ma (2013) to estimate a black hole mass of $\sim 10^{7.1}$ M_\odot , roughly a factor of three higher than that estimated by van Velzen et al. (2019), although these methods use different data and scaling relations.

Our photometric follow-up campaign includes several filters for which archival imaging data are not available, including the *Swift* UVOT and *BV* filters. In order to estimate the host flux in these filters for host flux subtraction, we convolved the host SED from FAST with the filter response curve for each filter to obtain $15''0$ fluxes. To estimate uncertainties on the estimated host galaxy fluxes, we perturbed the archival host fluxes assuming Gaussian errors and ran 1000 different FAST iterations. These synthetic fluxes were then used to subtract the host flux in our non-survey follow-up data.

The upper left panel of Figure 2 compares the $H\alpha$ emission line equivalent width to the Lick $H\delta_A$ absorption index, which compares current and past star formation to identify post-starburst galaxies. The upper right panel of 2 shows $H\alpha$ emission equivalent width as compared to $\log_{10}([NII]/H\alpha)$ to separate ionization mechanisms, particularly those associated with LINER-like (Low-Ionization Nuclear Emission-

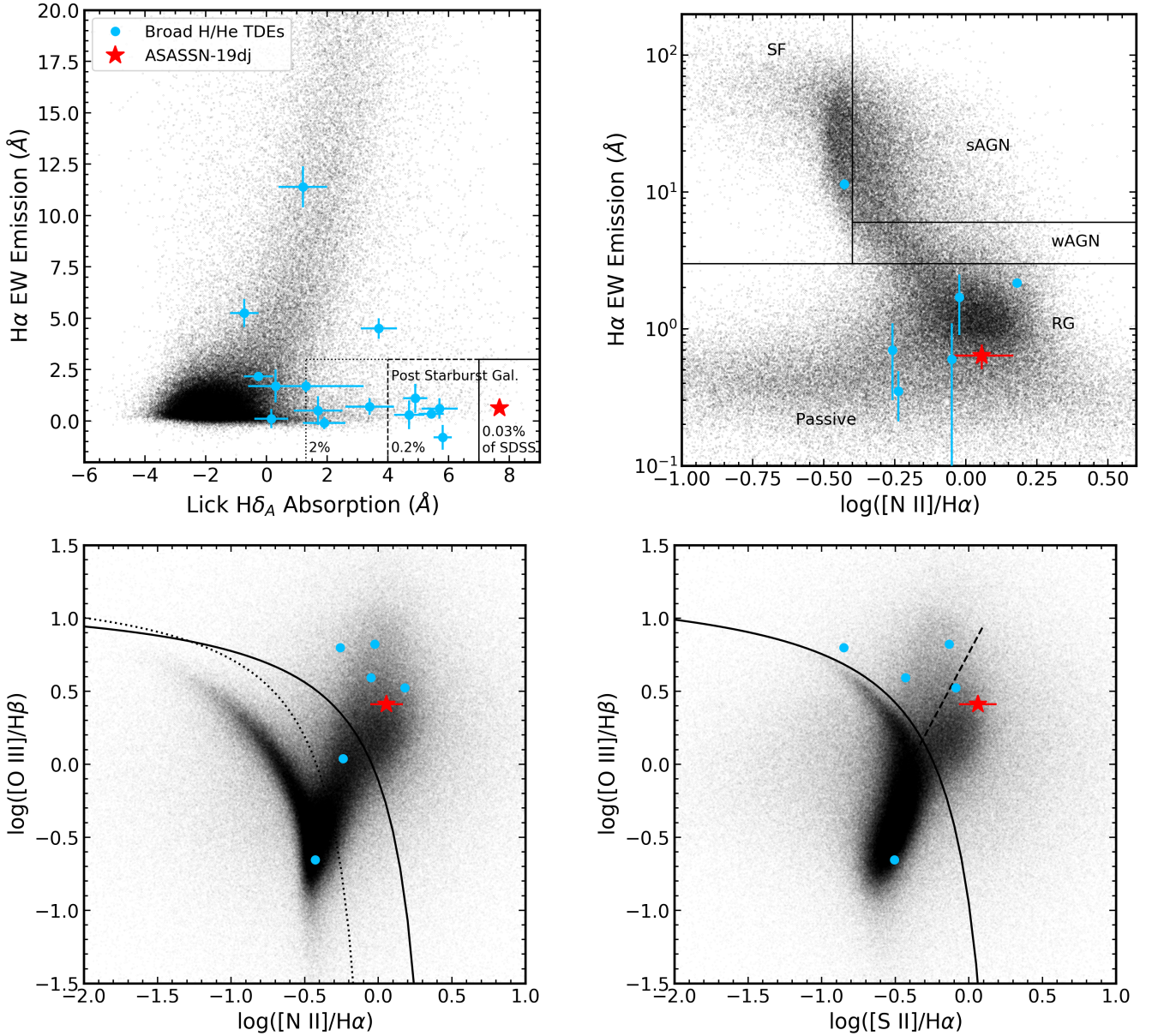


Figure 2. *Upper Left Panel:* $H\alpha$ emission line equivalent width (EW), which traces current star formation, as compared to the Lick $H\delta_A$ absorption index, which traces star formation in the past Gyr. The host galaxy KUG 0810+227 is shown as a red star, with other TDE hosts shown as blue circles. KUG 0810+227 is similar to some extreme post-starbursts galaxies seen in SDSS. The error bars on KUG 0810+227 are roughly the size of the symbol. *Upper Right Panel:* $H\alpha$ emission line equivalent width ($W_{H\alpha}$), as compared to $\log_{10}([N II] / H\alpha)$, otherwise known as the WHAN diagram (Cid Fernandes et al. 2011). Lines separating star-forming galaxies (SF), strong AGN (sAGN), weak AGN (wAGN), and passive and “retired galaxies” (RG) are shown (Cid Fernandes et al. 2011). *Lower Left Panel:* $\log_{10}([O III] / H\beta)$ vs. $\log_{10}([N II] / H\alpha)$ diagram (Baldwin et al. 1981; Veilleux & Osterbrock 1987). The solid line is the theoretical line separating AGN (above right) and H II-regions (below left) from Kewley et al. (2001). The dotted line is the empirical line from Kauffmann et al. (2003) showing the same separation. Objects between the dotted and solid lines are classified as composites. *Lower Right Panel:* $\log_{10}([O III] / H\beta)$ vs. $\log_{10}([S II] / H\alpha)$ diagram (Veilleux & Osterbrock 1987). The solid line is the theoretical line separating AGN (above right) and H II-regions (below left) from Kewley et al. (2001). The diagonal dashed line is the theoretical line separating Seyferts (above left) and LINERs (below right) from Kewley et al. (2006). KUG 0810+227 appears in the LINER region of both diagrams. In all panels, galaxies from SDSS Data Release 8 (Eisenstein et al. 2011) are shown in black.

line Region) emission line ratios. The bottom two panels of Figure 2 show $\log_{10}([O III]/H\beta)$ vs. $\log_{10}([N II]/H\alpha)$ and $\log_{10}([O III]/H\beta)$ vs. $\log_{10}([S II]/H\alpha)$ to characterise the activity of the host galaxies of TDEs. The background points in these figures are taken from the MPA-JHU catalog (Brinch-

mann et al. 2004), which calculated the spectral properties of galaxies in SDSS DR8 (Eisenstein et al. 2011).

We obtained the archival SDSS (York et al. 2000) spectrum of KUG 0810+227. This spectrum shows $[N II] \lambda 6584$, $[S II] \lambda \lambda 6717, 6731$, $[O I] \lambda 6300$, and $[O III] \lambda \lambda 4959, 5007$ in

emission with weak $H\alpha$ emission and $H\beta$ in absorption. The line ratios $\log_{10}([O III]/H\beta) = 0.41$, $\log_{10}([N II]/H\alpha) = 0.07$, $\log_{10}([S II]/H\alpha) = 0.06$, and $\log_{10}([O I]/H\alpha) = -0.59$ place this galaxy in the LINER (Low-Ionization Nuclear Emission-line Region) part of the Baldwin et al. (1981) and Veilleux & Osterbrock (1987) diagrams ($[N II]/H\alpha$, $[S II]/H\alpha$, and $[O I]/H\alpha$ vs. $[O III]/H\beta$). LINER-like line ratios may be produced by a variety of physical processes including ionization by shocks (e.g., Rich et al. 2015), AGN photoionization with a low ionization parameter (e.g. Groves et al. 2004; Kewley et al. 2006), or ionization by an older stellar population (e.g., Sarzi et al. 2005). The WHAN diagram of Figure 2 places KUG 0810+227 in the “retired galaxies” (RG) region, where galaxies have ceased actively forming stars and are predominantly ionised by hot low-mass evolved stars such as post-AGB stars (Cid Fernandes et al. 2011). We note that other TDE hosts also tend to populate the RG region of this diagnostic diagram. Thus, while KUG 0810+227 may harbor a LLAGN, it is also possible that other processes are at play in its LINER-like line ratios.

From Figure 2, we see that KUG 0810+227 is a post-starburst galaxy. The archival SDSS spectrum displays weak $H\alpha$ emission and extremely strong $H\delta$ absorption, with a Lick $H\delta_A$ index of 7.67 ± 0.17 Å as measured by Brinchmann et al. (2004), providing confirmation of this classification. This is consistent with the tendency for TDEs to be found in post-starburst, or “quiescent Balmer-strong”, host galaxies (e.g., Arcavi et al. 2014; French et al. 2016; Law-Smith et al. 2017). Additionally, the host of ASASSN-19dj is similar to many other TDE hosts in terms of its star formation history. Compared to other TDE hosts, KUG 0810+227 is similar in its line ratios, although the low-ionization line ratios are slightly higher than the rest, potentially suggesting the contribution of shocks. The possibility that KUG 0810+227 hosts an LLAGN is in line with the fact that hosts of other TDE such as ASASSN-14ae (Holoien et al. 2014a), ASASSN-14li (Holoien et al. 2016b; French et al. 2020), ASASSN-19bt (Holoien et al. 2019b), show evidence for weak AGN activity.

The fact that KUG 0810+227 has both LINER-like line ratios and is a RG is in line with several studies on the ionization processes in post starburst galaxies. De Propriis & Melnick (2014) compiled a sample of ten post-starburst galaxies with Hubble Space Telescope (HST) imaging, optical spectra, X-ray, far-infrared, and radio data. They found no evidence of AGN down to an Eddington ratio of 0.1% in these galaxies. Similarly, French et al. (2018) found that many post-starburst galaxies have LINER-like line ratios, and that most are in the RG region of the WHAN diagram. The TDE hosts in particular have lower $H\alpha$ EW, placing them solidly in the RG region (French et al. 2017). However, Prieto et al. (2016) suggests that the host galaxy of the TDE ASASSN-14li, which we note is a RG in the WHAN diagram, may host an AGN.

Archival Catalina Real-Time Transient Survey (CRTS; Drake et al. 2009) data indicates that KUG 0810+227 experienced an outburst at MJD ~ 53640 (September 2005), roughly 14.5 years prior to ASASSN-19dj. We obtained photometric data for this flare from both the Catalina Sky Survey (CSS) 0.7-m and the Mount Lemmon Survey (MLS) 1.5-m telescopes. First, we fit a flat line to the CRTS data between MJD = 54592 and MJD = 55919, outside of the

flare to obtain a flux zero point. The zero-point-subtracted light curve and a comparison of the flare to ASASSN-19dj are shown in Figure 3. The reduced chi-squared of the non-outburst parts of the CRTS light curve as compared to the zero-point fit is 1.38, indicating that the V-band light curve is non-variable. The flare in CRTS appears to be of a similar magnitude to ASASSN-19dj, though we note that the peak of the CRTS flare may have occurred in the seasonal gap. The FWHM (full width at half maximum) of the ASASSN-19dj flare is ~ 80 days in the ASAS-SN g-band data, while the FWHM of the CRTS flare is $\lesssim 140$ days, although we do not see the full rise or peak of this flare. Finally, the light curve of ASASSN-19dj appears to decline slower than the CRTS flare as indicated by the right panel of Figure 3.

The photometry from CRTS uses SExtractor (Bertin & Arnouts 1996), which includes flux from the entire host galaxy. Thus it is not possible to determine the nature of the transient from the CRTS photometry alone. In an effort to link this flare to a known transient, we searched multiple databases of known supernovae such as the Open Supernova Project (Guillochon et al. 2017b) and the Central Bureau for Astronomical Telegrams (CBAT³) but found no reported SNe or other flares at the time. Nevertheless, even if the source is consistent with the nucleus, it is difficult to constrain the nature of the earlier transient without spectroscopic or multi-band photometric observations during that epoch.

2.2 ASAS-SN Light Curve

ASAS-SN is a fully automated transient survey which consists of 20 telescopes on 5 robotic mounts. Each telescope is a 14-cm aperture Nikon telephoto lens with 8''0 pixels, and each unit consists of 4 telescopes on a common mount. Single ASAS-SN units are located at Haleakalā Observatory, McDonald Observatory, and the South African Astrophysical Observatory (SAAO), and two are located at Cerro Tololo Inter-American Observatory (CTIO). With our current network, ASAS-SN monitors the visible sky with a cadence of ~ 20 hours to a depth of $g \sim 18.5$ mag.

Since ASASSN-19dj is near the equator, it was observed from both hemispheres and by all 5 units. Additionally, ASASSN-19dj lies in a designed 0.5 degree field overlap region, giving us roughly twice the cadence. Thus we observed ASASSN-19dj with 10 of the 20 ASAS-SN cameras currently deployed. However, the filters for two of the ASAS-SN units, Brutus and Cassius, had been changed from V to g shortly before ASASSN-19dj was discovered. Thus, there were not enough g-band images taken before the TDE to construct a subtraction reference image for those cameras. Because of this we had to modify the normal ASAS-SN processing pipeline to extract the light curve.

Images were reduced using the automated ASAS-SN pipeline but we performed image subtraction separately. We used the ISIS image subtraction package (Alard & Lupton 1998; Alard 2000a) with the same parameters as the ASAS-SN pipeline, but images from all cameras for a given pointing were first interpolated onto a common grid. We then built a reference image using good images from multiple cameras

³ <http://www.cbat.eps.harvard.edu/lists/Supernovae.html>

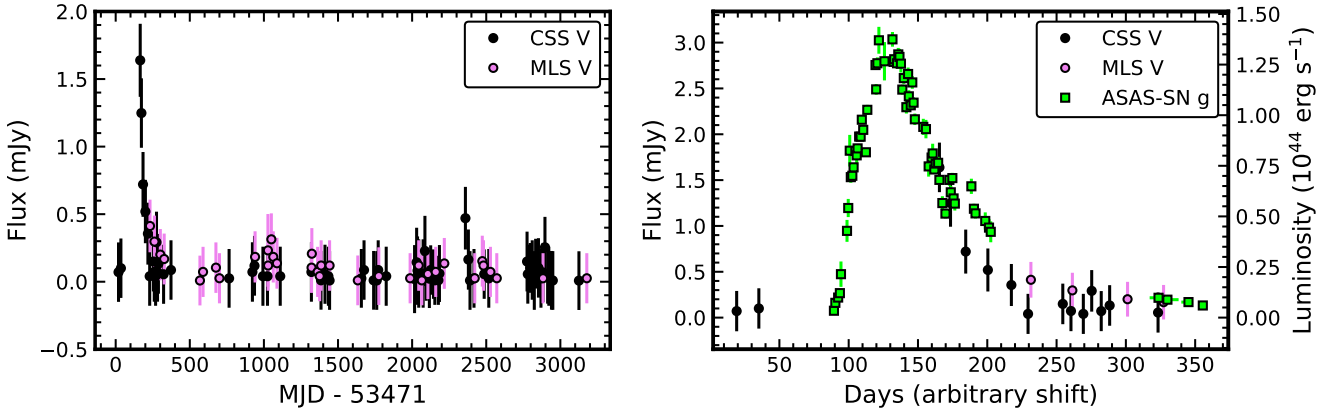


Figure 3. *Left Panel:* The V-band CRTS data (CSS in black and MLS in violet) light curves. *Right Panel:* Comparison of the flare seen at MJD ~ 53680 by CRTS and the ASASS-SN g-band data (shown in green) of the TDE ASASSN-19dj with an arbitrary shift in days between the two flares so that they are roughly aligned. The two light curves are offset by their best-fit zero-points and have been corrected for Galactic extinction.

observed well before the rise of ASASSN-19dj. This common reference image was used to analyze all the data.

We then used the IRAF `apphot` package with a 2-pixel radius (approximately $16''$) aperture to perform aperture photometry on each subtracted image, generating a differential light curve. The photometry was calibrated using the AAVSO Photometric All-Sky Survey (Henden et al. 2015). We visually inspected each of the 1155 exposures taken after 2018 February 5 analyzed in this work for clouds or flat-fielding issues and disregarded any where issues were seen. We also discarded images with a FWHM of 1.67 pixels or greater.

To increase the signal-to-noise ratio (S/N) we stacked our photometric measurements. For exposures with TDE emission, the photometric measurements were stacked in 12 hour bins. Prior to our first detection, measurements within 75 hours of each other were stacked to get deeper upper limits. After the 2019 seasonal gap, measurements within 10 days of each other were stacked to sample the decline of the TDE.

2.3 ATLAS light curve

The ATLAS survey is designed primarily to detect small (10–140 m) asteroids that may collide with Earth (Tonry et al. 2018). ATLAS uses two 0.5m f/2 Wright Schmidt telescopes on Haleakalā and at the Mauna Loa Observatory. For normal operation, the telescopes obtain four 30-second exposures of 200–250 fields per night. This allows the telescopes to cover roughly a quarter of the sky visible from Hawaii each night, ideal for transient detection (Smith et al. 2020). ATLAS uses two broad-band filters, the ‘cyan’ (c) filter from 420–650 nm and the ‘orange’ (o) filter covering the 560–820 nm range (Tonry et al. 2018).

Each ATLAS image is processed by a pipeline that performs flat-field corrections in addition to astrometric and photometric calibrations. Reference images of the host galaxy were created by stacking multiple images taken under excellent conditions before MJD = 58251 and this reference was then subtracted from each science image of ASASSN-19dj in order to isolate the flux from the transient. We per-

formed forced photometry on the subtracted ATLAS images of ASASSN-19dj as described in Tonry et al. (2018). We combined the four intra-night photometric observations using a weighted average to get a single flux measurement. The ATLAS o-band photometry and 3-sigma limits are presented in Table 2 and are shown in Figure 4. We do not plot the c-band photometry in Figure 4 as there were few c-band observations in the rise to peak and near peak due to weather and the design of the ATLAS survey, but as they provide useful early limits and detections, we present them in Table 1.

2.4 ZTF Light Curves

The ZTF survey uses the Samuel Oschin 48” Schmidt telescope at Palomar Observatory and a camera with a 47 square degree field of view that reaches as deep as 20.5 *r*-band mag in a 30 second exposure. Alerts for transient detection from ZTF are created from the final difference images (Patterson et al. 2019). These alerts are distributed to brokers including Lasair (Smith et al. 2019) through the University of Washington Kafka system. For ASASSN-19dj, we obtained ZTF *g*- and *r*-band light curves from the Lasair broker⁴. Lasair uses ZTF difference imaging photometry so the host flux is subtracted. The ZTF magnitudes presented in this paper are calculated using PSF photometry. Similar to the ATLAS data, we combined the intra-night photometric observations using a weighted average to get a single flux measurement.

2.5 Additional Ground-Based Photometry

We also obtained photometric follow-up observations from several ground-based observatories. We used the Las Cumbres Observatory (Brown et al. 2013) 1-m telescopes located at CTIO, SAAO, McDonald Observatory, and Siding Spring Observatory for *BVgr*i observations, and the Swope 1-m telescope at Las Campanas Observatory for *uBVgr*i observations. After applying flat-field corrections, we solved astrom-

⁴ <https://lasair.roe.ac.uk/>

Table 2. Host-Subtracted Photometry of ASASSN-19dj

| MJD | Filter | Magnitude | Uncertainty | Telescope |
|----------|-------------|-----------|-------------|--------------|
| 58537.07 | <i>i</i> | 16.36 | 0.01 | LCOGT-1m |
| 58539.86 | <i>i</i> | 16.24 | 0.01 | LCOGT-1m |
| 58541.81 | <i>i</i> | 16.12 | 0.01 | LCOGT-1m |
| ... | ... | ... | ... | ... |
| 58850.21 | <i>UVW2</i> | 17.68 | 0.07 | <i>Swift</i> |
| 58906.65 | <i>UVW2</i> | 17.74 | 0.11 | <i>Swift</i> |
| 58911.89 | <i>UVW2</i> | 18.00 | 0.18 | <i>Swift</i> |

Host-subtracted magnitudes and 3σ upper limits for all follow-up photometry. A range of MJD in the first column indicates the beginning and end of the range over which data were stacked to increase S/N. All magnitudes are corrected for Galactic extinction and presented in the AB system. The last column reports the source of the data for each epoch. The *Swift* *B* data do not include the shift applied in Figure 4. Only a small section of the table is displayed here. The full table can be found online as an ancillary file.

etry in each image using astrometry.net (Barron et al. 2008; Lang et al. 2010).

We aligned the *ugri* data to the archival SDSS image in the corresponding filter for each follow-up image using the Python `reproject` package, which uses the WCS information of two images to project one image onto the other. We then subtracted the SDSS template images from each follow-up image using HOTPANTS⁵ (Becker 2015), an implementation of the Alard (2000b) image subtraction algorithm, and used the IRAF `apphot` package to measure $5''.0$ aperture magnitudes of the transient. For the *BV* data, we did not have archival images available to use as subtraction template images. Instead, we used `apphot` to measure $15''.0$ aperture magnitudes of the host + transient, and subtracted the $15''.0$ host flux synthesised from our FAST fit in the appropriate filter to isolate the transient flux. For all filters, we used SDSS stars in the field to calibrate our photometry, using the corrections from Lupton (2005) to calibrate the *B* and *V* band magnitudes with the *ugriz* data.

We measured the centroid position of the transient in a host-subtracted Las Cumbres Observatory *g*-band image taken near peak using the IRAF `imcentroid` package. This yielded a position of $(\alpha, \delta) = (08:13:16.96, +22:38:54.00)$. We also used the archival SDSS *g*-band image to measure the position of the nucleus of KUG 0810+227, finding $(\alpha, \delta) = (08:13:16.95, +22:38:53.89)$. This gives an angular offset of $0''.21 \pm 0''.12$, where the uncertainty is due to uncertainty in the centroid positions of the TDE and host nucleus. We also measured the centroid positions of several stars in both the follow-up and SDSS host images, finding that the stars had an average random offset of $0''.19$. Combining these sources of uncertainty, the transient position is thus offset $0''.21 \pm 0''.24$ from the position of the host nucleus, corresponding to a physical distance of 99.2 ± 112.5 pc.

2.6 *Swift* Observations

Forty-four total Neil Gehrels Swift Gamma-ray Burst Mission (*Swift*; Gehrels et al. 2004) target-of-opportunity (ToO) observations were carried out between 2019 March 2 and 2020 March 3 (Swift target ID 11186 (as AT2019azh; PIs: Gezari, Arcavi, and Wevers), and Swift target ID 12174 (as ASASSN-19dj; PI: Hinkle). These observations used the UltraViolet and Optical Telescope (UVOT; Roming et al. 2005) and X-ray Telescope (XRT; Burrows et al. 2005) to study the multi-wavelength properties of the TDE.

2.6.1 UVOT Observations

For a majority of the observation epochs, *Swift* observed ASASSN-19dj with all six UVOT filters (Poole et al. 2008): *V* (5468 Å), *B* (4392 Å), *U* (3465 Å), *UVW1* (2600 Å), *UVM2* (2246 Å), and *UVW2* (1928 Å). Each epoch of UVOT data includes 2 observations in each filter, which we combined into one image for each filter using the HEASoft `uvotimsum` package. We then used the `uvotsource` package to extract source counts using a $15''.0$ radius region centered on the position of the TDE and background counts using a source-free region with radius of $\sim 40''.0$. We converted the UVOT count rates into fluxes and magnitudes using the most recent calibrations (Poole et al. 2008; Breeveld et al. 2010).

Because the UVOT uses unique *B* and *V* filters, we used publicly available colour corrections⁶ to convert the UVOT *BV* data to the Johnson-Cousins system. We then corrected the UVOT photometry for Galactic extinction and removed host contamination by subtracting the corresponding $15''.0$ host flux in each filter, as we did with the ground-based *BV* data.

Figure 4 shows the extinction-corrected, host-subtracted light curves of ASASSN-19dj. The photometry spans from the shortest *UVW2* (1928 Å) band of Swift to *i*-band (~ 7609 Å) from Swope and LCOGT and includes the data ranging from 21 days prior to peak to 392 days after peak. The corrected *Swift B* data were inconsistent with the ground-based *B* data, so we shifted the *Swift B* data in Figure 4. To do this, we computed the average of the offset between the peaks of the LCOGT and Swope *B*-band data from the *Swift B* data, which was found to be 0.16 mag. All the UV and optical photometry shown in Figure 4, in addition to limits not shown in this figure, is presented in Table 2.

2.6.2 XRT Observations

In addition to the *Swift* UVOT observations, we also obtained simultaneous *Swift* X-Ray Telescope (XRT) photon-counting observations. All observations were reprocessed from level one XRT data using the *Swift* XRTPIPELINE version 0.13.2, producing cleaned event files and exposure maps. Standard filter and screening criteria⁷ were used, as well as the most up-to date calibration files.

⁵ <http://www.astro.washington.edu/users/becker/v2.0/hotpants.html>

⁶ https://heasarc.gsfc.nasa.gov/docs/heasarc/caldb/swift/docs/uvot/uvot_caldb_coltrans_02b.pdf

⁷ http://swift.gsfc.nasa.gov/analysis/xrt_swguide_v1_2.pdf

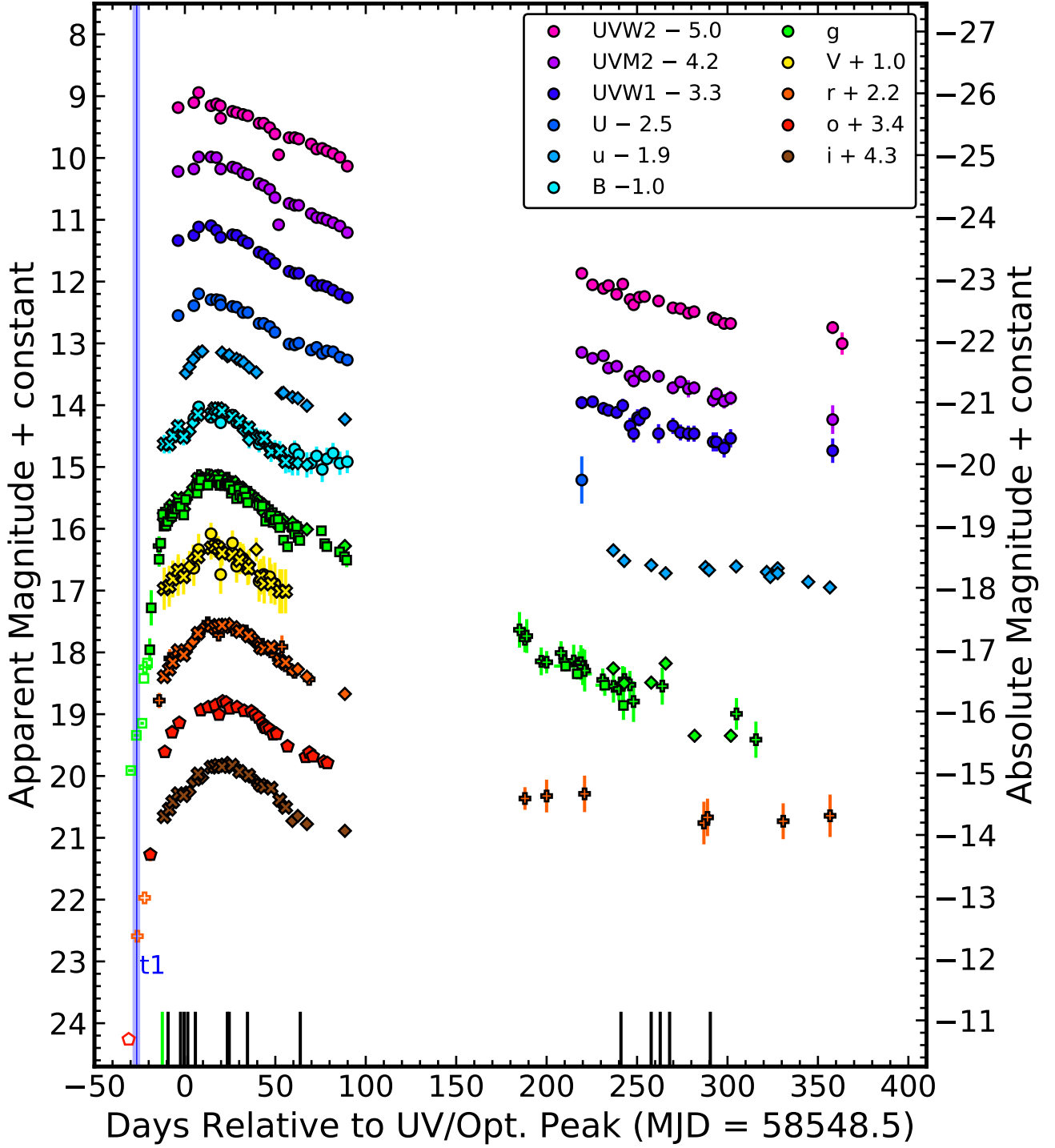


Figure 4. Host-subtracted UV and optical light curves of ASASSN-19dj, showing ASAS-SN (g , squares), Swift (UV+ UBV , circles), ATLAS (o , pentagons), ZTF (gr , pluses), Swope ($uBVgri$, diamonds), and Las Cumbres Observatory 1-m telescopes ($BVgri$, x-shapes) photometry spanning from roughly 20 days prior to peak (MJD = 58548.5) to roughly 390 days after in observer-frame days. Horizontal error bars on the ASAS-SN g -band data indicate the date range of observations stacked to obtain deeper limits and higher S/N detections, although they are small and difficult to see. Open symbols indicate 3σ upper limits when the TDE was not detected. The green bar on the x-axis marks the epoch of ASAS-SN discovery. Black bars along the x-axis show epochs of spectroscopic follow-up. The blue line is the estimated time of first light (see §3.1) with the shading corresponding to the uncertainty. All data are corrected for Galactic extinction and shown in the AB system.

To extract both background-subtracted count rates and spectra, we used a source region with a radius of $50''$ centered on the position of ASASSN-19dj and a source free background region centered at $(\alpha, \delta) = (08^h 13^m 07.93^s, +22^\circ 35' 15.36'')$ with a radius of $150''.0$. The reported count rates are aperture corrected where a $50''$ source radius contains $\sim 90\%$ of the source counts at 1.5 keV , assuming an on-axis pointing (Moretti et al. 2004). To increase the S/N of our observations, we combined our individual *Swift* observations into six time bins using XSELECT version 2.4g, allowing us to extract spectra with $\gtrsim 200 - 300$ background subtracted counts.

To extract spectra from our merged observations, we used the task XRTPRODUCTS version 0.4.2 and the regions defined above to extract both source and background spectra. To extract ancillary response files (ARF), we first merged the corresponding individual exposure maps that were generated by XRTPipeline using XIMAGE version 4.5.1 and then used the task XRTMKARF. We used the ready-made response matrix files (RMFs) that are available with the *Swift* calibration files. Each spectrum was grouped to have a minimum of 10 counts per energy bin using the FTOOLS command GRPPHA.

2.7 NICER Observations

After the 2019 seasonal gap, follow-up *Swift* XRT observation found that the X-ray flux of ASASSN-19dj had increased by an order of magnitude compared to the flux approximately 100 days earlier (see §3.5). ToO observations of ASASSN-19dj were obtained using the Neutron star Interior Composition Explorer (NICER: Gendreau et al. 2012), which is an external payload on the International Space station that has a large effective area over the $0.2\text{--}12.0\text{ keV}$ energy band and provides fast X-ray timing and spectroscopic observations of sources. In total, 80 observations were taken between 2019 October 23 and 2020 March 12 (Observation IDs: 2200920101–2200920176, 3200920101–3200920105, PI: Pasham/Gendreau, Pasham et al. 2019), totaling 169 ks of cumulative exposure.

The data were reduced using NICERDAS version 6a, HEASOFT version 6.26.1. Standard filtering criteria were applied using the NICERDAS task NICERL2. Here the standard filter criteria includes⁸: the *NICER* pointing is (ANG_DIST) < 0.015 degrees from the position of the source; excluding events that were acquired during passage through the South Atlantic Anomaly, or those that are obtained when Earth was 30° (40°) above the dark (bright) limb (ELV and BR_EARTH, respectively). We also removed events that are flagged as overshoot, or undershoot events (EVENT_FLAGS=bxxxx00), and we used the so-called “trumpet filter” to remove events with a PLRATIO $> 1.1 + 120/\text{PI}$, where PI is the pulsar invariant amplitude of an event, as these are likely particle events (Bogdanov et al. 2019). To extract time-averaged spectra and count rates, we used XSELECT, and ready made ARF (nxtiaveonaxis20180601v002.arf) and

RMF (nxtiref20170601v001.rmf) files that are available with the *NICER* CALDB. Similar to the *Swift* spectra, each spectrum was grouped with a minimum of 10 counts per energy bin. As *NICER* is a non-imaging instrument, background spectra were generated using the background modeling tool NIBACKGEN3C50⁹.

To analyse the spectra extracted from both our *Swift* and *NICER* observations, we used the X-ray spectral fitting package (XSPEC) version 12.10.1f (Arnaud 1996) and χ^2 statistics. Both the *Swift* and *NICER* data and their analysis are further discussed in §3.5.

2.8 XMM-Newton slew observations

In addition to *Swift* and *NICER* observations, we also searched for *XMM-Newton* slew observations that overlap the position of ASASSN-19dj. These slew observations are taken using the PN detector of *XMM-Newton* as it maneuvers between pointed observations, detecting X-ray emission down to a $0.2\text{--}10.0\text{ keV}$ flux limit of $\sim 10^{-12}\text{ erg cm}^{-2}\text{ s}^{-1}$ (Saxton et al. 2008). We found two slew observations (ObsIDs: 9353900003 and 9363000003) coincident with the position of ASASSN-19dj. These observations were taken on 2019-04-07 and 2019-10-05, respectively, corresponding to ~ 44 and ~ 225 days after discovery. To analyse these observations we follow the current slew analysis thread on the *XMM-Newton* Science System (SAS) data analysis threads¹⁰. Here we use the SAS tool command ESLEWCHAIN and the most up to date calibration files to produce filtered event files that we use in our analysis. Similar to our *XRT* analysis, we extract the number of counts using a source region with a radius of $30''$ centered on the position of ASASSN-19dj and a source free background region with a radius of $150''$ centered at $(\alpha, \delta) = (08^h 13^m 31^s.79, +22^\circ 37' 30''.53)$. A $30''$ source region contains 85% of all source photons at 1.9 keV . Due to the low exposure times of each observation, which was determined using the corresponding exposure files of each observation, no spectra could be extracted. The $0.3 - 10\text{ keV}$ X-ray luminosities and hardness ratios derived from the count rates for the various X-ray epochs are shown in Table 3.

2.9 Spectroscopic Observations

In addition to the ePESSTO spectrum released on TNS, we obtained follow-up spectra of ASASSN-19dj with LDSS-3 on the 6.5-m Magellan Clay telescope, the Inamori-Magellan Areal Camera and Spectrograph (IMACS; Dressler et al. 2011) on the 6.5-m Magellan-Baade telescope, the Wide Field Reimaging CCD Camera (WFCCD) on the du Pont 100-inch telescope, the SuperNova Integral Field Spectrograph (SNIFS; Lantz et al. 2004) on the 88-inch University of Hawaii telescope, the Low-Resolution Imaging Spectrometer (LRIS; Oke et al. 1995) on the 10-m Keck I telescope, and the Multi-Object Double Spectrographs (MODS; Pogge et al. 2010) on the Large Binocular Telescope (LBT;

⁸ See https://heasarc.gsfc.nasa.gov/docs/nicer/data_analysis/nicer_analysis_guide.html or (Bogdanov et al. 2019) for more details about these criteria.

⁹ https://heasarc.gsfc.nasa.gov/docs/nicer/tools/nicer_bkg_est_tools.html

¹⁰ <https://www.cosmos.esa.int/web/xmm-newton/sas-thread-epic-slew-processing>

Table 3. X-ray Luminosity and Hardness Ratios of ASASSN-19dj

| MJD | log Lum. (erg s ⁻¹) | Lum. Error (erg s ⁻¹) | HR | HR Error | Satellite |
|----------|------------------------------------|--------------------------------------|-------|----------|--------------|
| 58544.76 | 40.72 | — | -0.07 | — | <i>Swift</i> |
| 58553.45 | 41.42 | 0.23 | -0.53 | 0.28 | <i>Swift</i> |
| 58556.11 | 41.36 | 0.26 | -1.00 | 0.01 | <i>Swift</i> |
| ... | ... | ... | ... | ... | |
| 58922.58 | 42.06 | 0.04 | -0.70 | 0.09 | <i>NICER</i> |
| 58934.02 | 42.03 | 0.06 | -0.63 | 0.11 | <i>NICER</i> |
| 58940.53 | 41.96 | 0.06 | -0.40 | 0.07 | <i>NICER</i> |

X-ray luminosities and hardness ratios with associated uncertainties. Dashed lines represent 3σ upper limits. The hardness ratio is defined as $(H-S)/(H+S)$, where we define hard counts H as the number of counts in the 2-10 keV range and soft counts S are the number of counts in the 0.3-2 keV. The last column reports the source of the data for each epoch. Only a small section of the table is displayed here. The full table can be found online as an ancillary file.

Hill et al. 2006). Three of our spectra were obtained prior to peak light and eleven were obtained after peak. Most of the spectra were reduced and calibrated with standard IRAF procedures, such as bias subtraction, flat-fielding, 1-D spectroscopic extraction, and wavelength calibration. The IMACS data from 2019 November 19.3 were reduced using an updated version of the routines developed by Kelson et al. (2014). The flux calibration for our observations was initially done using standard star spectra obtained on the same nights as the science spectra and then refined using our follow-up photometry.

All the classification and follow-up spectra for ASASSN-19dj are presented in Figure 5. From top to bottom, the optical spectrum evolves from a hot, blue continuum to a host-dominated spectrum. The locations of several emission lines commonly seen in TDEs are marked with vertical dashed lines. Some of these emission lines appear, evolve, and disappear throughout the time period probed by these spectra.

3 ANALYSIS

3.1 Light Curve

Using Markov Chain Monte Carlo (MCMC) methods, we fit each of the epochs where there is *Swift* UV photometry as a blackbody to obtain the bolometric luminosity, temperature, and effective radius of ASASSN-19dj. So that our fits are relatively unconstrained, we ran each of our blackbody fits with flat temperature priors of $10000 \text{ K} \leq T \leq 55000$. To find the time of peak UV/optical luminosity, we fit a parabola to the light curve created by bolometrically correcting the ASASSN g-band light curve using these blackbody fits. For this fit, we excluded any upper limits. Because the curve is quite flat near peak, we fit the parabola in a narrow range between $\text{MJD} = 58535.2$ and $\text{MJD} = 58556.2$. We generated 10,000 realizations of the bolometric light curve in this date range with each magnitude perturbed by its uncertainty assuming Gaussian errors. We then fit a parabola to each of these light curves and took the median value as the peak and 16th and 84th percentiles as the uncertainties in peak time. Using this

procedure, we find the time of peak bolometric luminosity to be $\text{MJD} = 58548.5^{+6.3}_{-2.6}$. From Figure 4, looking from the shortest wavelength (*UVW2*) to the longest (*i*), we see that the time of peak light in each band is offset from each other. Using a similar procedure to the bolometric lightcurve, but for the flux in a single photometric band, we find that the *Swift* *UVW2* light curve peaks at $\text{MJD} = 58554.9^{+1.1}_{-1.5}$ and the LCOGT *i*-band light curve peaks at $\text{MJD} = 58571.9 \pm 0.1$. This offset of ~ 17 days is longer than the offsets seen in other TDEs such as ASASSN-18pg (Holoien et al. 2020) and ASASSN-19bt (Holoien et al. 2019b). This likely occurs because the temperature of ASASSN-19dj steadily declines for roughly 25 days before increasing for 20 days and gradually leveling off for the next ~ 230 days (see §3.3), in contrast with some TDEs that exhibit relatively flat temperature evolution near peak (e.g., Hinkle et al. 2020; van Velzen et al. 2020).

ASASSN-19dj is one of only a few TDEs for which the early-time coverage is adequate to fit a rise slope. We fit the early-time rise as a power-law with

$$f = z \text{ for } t < t_1, \text{ and} \quad (1)$$

$$f = z + h \left(\frac{t - t_1}{\text{days}} \right)^\alpha \text{ for } t > t_1 \quad (2)$$

This model fits for the zero point z , the time of first-light t_1 , a flux scale h , and the power-law index α . An MCMC fit yields the best fit parameters $z = -30.7^{+8.6}_{-9.2} \mu\text{Jy}$, $h = 7.4^{+14.0}_{-5.5} \mu\text{Jy}$, $t_1(\text{MJD}) = 58521.9^{+1.3}_{-1.7}$, and $\alpha = 1.90^{+0.42}_{-0.36}$. These fits are shown in Figure 6. From this figure, we see that the light curve rises from the time of first light to the peak UV/optical bolometric luminosity in 26 days, shorter than the rise to peak time measured for ASASSN-19bt (Holoien et al. 2019b) and the limits on rise times for PS18kh (Holoien et al. 2019a), and ASASSN-18pg (Holoien et al. 2020). This may indicate a more efficient circularization of material for ASASSN-19dj. From the fitted time of first light, we find that ASAS-SN discovered this transient within about two weeks of the beginning of the flare.

ASASSN-19dj is only the second TDE for which a power-law could be fit to the early-time light curve. This best-fit power-law index of $\alpha = 1.90^{+0.42}_{-0.36}$ is consistent with the fireball model used for the early-time evolution of SNe (e.g., Riess et al. 1999; Nugent et al. 2011). ASASSN-19bt, the TDE with the best early-time data, and the only other TDE for which this has been done, also has a rise consistent with this model (Holoien et al. 2019b). Unlike the model invoked for SNe, where the ejecta initially expands at a constant velocity and temperature, the early stages of a TDE are more complex, so it is somewhat odd that these two objects have shown such a rise. Further analysis of more early-time TDE light curves will help us better understand their rise slopes. Finally, we note that the ASAS-SN g-band light curve follows a t^2 power-law rise for approximately 16 days, similar to ASASSN-19bt (Holoien et al. 2019b).

We used the Modular Open-Source Fitter for Transients (MOSFiT; Guillochon et al. 2017a; Mockler et al. 2019) to fit the host-subtracted light curves of ASASSN-19dj to estimate physical parameters of the star, SMBH, and the encounter. MOSFiT uses models containing several physical parameters to generate bolometric light curves of a transient, generates

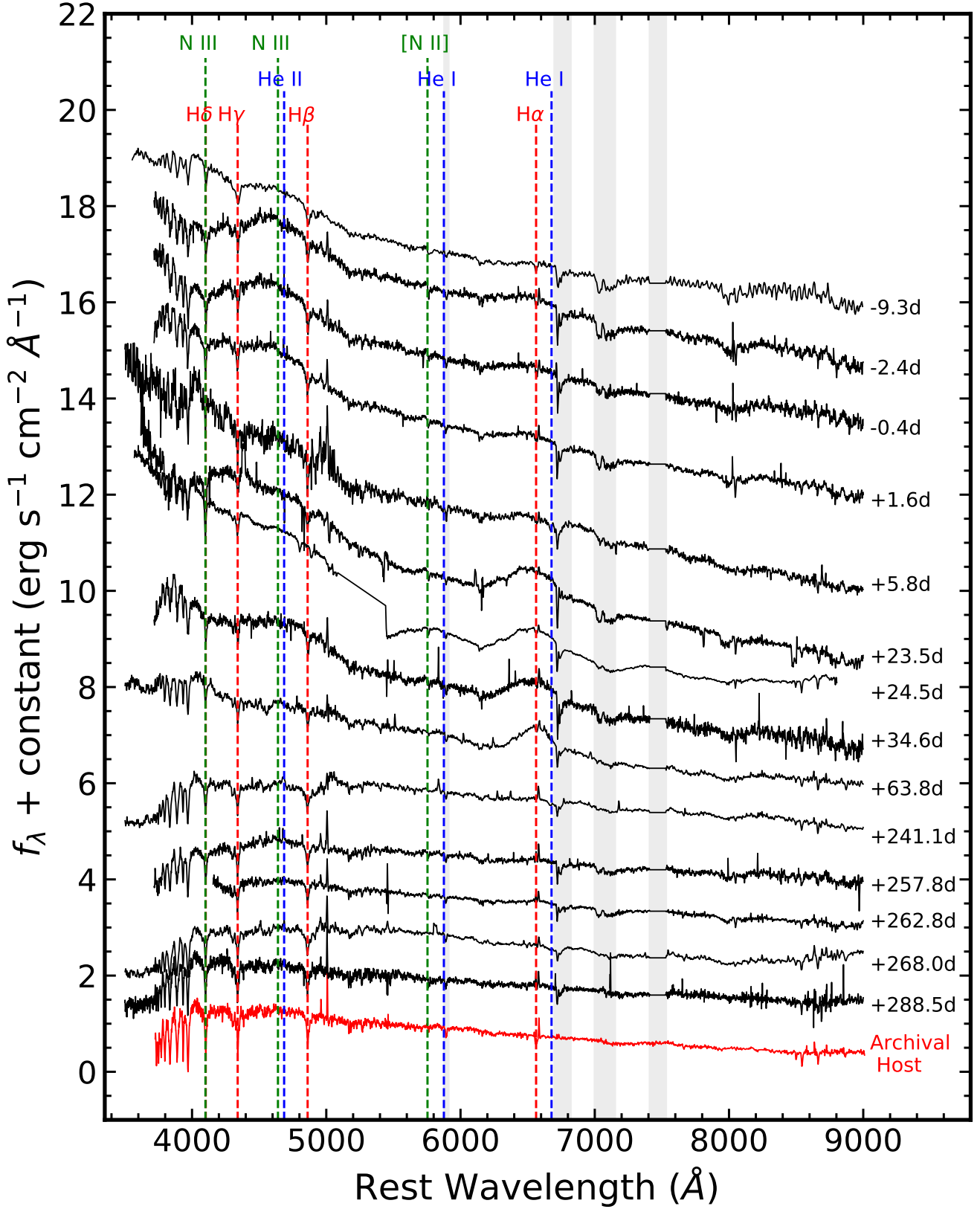


Figure 5. Optical spectroscopic evolution of ASASSN-19dj spanning from 9.3 days prior to peak UV/optical emission (top) until 288.5 days after peak (bottom). These spectra are calibrated using the photometry presented in Figure 4. The vertical gray bands mark atmospheric telluric features and the strong telluric feature between $\sim 7400 - 7550 \text{ \AA}$ has been masked. An archival host spectrum from SDSS is shown in red at the very bottom. The vertical lines mark spectral features common in TDEs, with hydrogen lines in red, helium lines in blue, and nitrogen lines in green. The straight line in the spectrum at 24.5 days after peak connects the blue and red sides of the LRIS spectrum with a large dichroic feature.

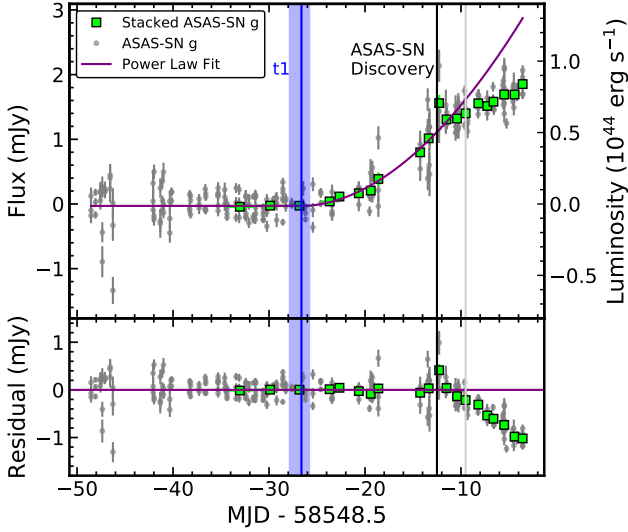


Figure 6. *Top panel:* Stacked (green) and raw (gray) ASASSN g-band light curve and best-fit power-law model in purple. This power-law fit yields a time of first light of $t_1 = 58521.9^{+1.3}_{-1.7}$ and a power-law index of $\alpha = 1.90^{+0.42}_{-0.36}$. The blue line shows the fitted time of first light with the shading representing the uncertainty and the black line shows the ASASSN discovery date. The light gray line marks the last epoch that was fit by our MCMC model. *Bottom panel:* Residuals between the data and best-fit power-law model. The ASASSN g-band light curves deviates from a power-law rise roughly 16 days after the fitted time of first light.

single-filter light curves from the bolometric light curves, and fits these to the observed multi-band data. It then finds the combination of parameters yielding the highest likelihood match for a given model using one of various sampling methods. We ran the MOSFiT TDE model in nested sampling mode when fitting our data, as we have a large number of observations in several photometric filters.

MOSFiT is the only available tool for generalised fitting of TDE emission, and seems to model cases such as ASASSN-19dj, which has relatively smooth light curves, fairly well. We show the MOSFiT multi-band fits to the ASASSN-19dj light curves in Figure 7 with our data overplotted. MOSFiT is able to fit the late-time data quite well, and does a reasonable job of fitting the data near the peak, particularly in the optical, though it slightly underestimates the UV emission near peak. The rise is particularly well constrained compared to many of the TDEs in the sample fit by Mockler et al. (2019) due to the high-cadence survey data in our dataset.

Table 4 shows the median values and 1 – 99% range for the MOSFiT TDE model parameters. The model parameters are generally very well constrained, with statistical uncertainties from the fit being significantly smaller than the systematic uncertainties of the model (see Table 3 of Mockler et al. 2019). The black hole mass and stellar mass given by MOSFiT are $M_h = 7.8^{+3.9}_{-4.1} \times 10^6 M_\odot$ and $M_\star = 0.10^{+0.37}_{-0.08} M_\odot$, respectively. This black hole mass is larger than, but marginally consistent with, the mass limit calculated by van Velzen et al. (2019) and consistent with our estimate in §2.1. The stellar mass, while low, is consistent with several other TDEs modelled in Mockler et al.

Table 4. MOSFiT TDE Model Parameter Fits

| Quantity | Value | Units |
|------------------------------|---------------------------|------------------|
| $\log R_{ph0}$ | $0.23^{+0.43}_{-0.42}$ | — |
| $\log T_{viscous}$ | $-0.09^{+0.39}_{-0.56}$ | days |
| b (scaled β) | $0.99^{+0.25}_{-0.93}$ | — |
| $\log M_h$ | $6.89^{+0.22}_{-0.71}$ | M_\odot |
| $\log \epsilon$ (efficiency) | $-0.44^{+0.71}_{-0.70}$ | — |
| l (photosphere exponent) | $1.84^{+0.27}_{-0.27}$ | — |
| $\log n_{H,host}$ | $20.71^{+0.02}_{-0.02}$ | cm^{-2} |
| M_\star | $0.10^{+0.37}_{-0.08}$ | M_\odot |
| t_{exp} | $-9.09^{+15.98}_{-15.86}$ | days |
| $\log \sigma$ | $-0.68^{+0.01}_{-0.01}$ | — |

Best-fit values and 1 – 99% ranges for the MOSFiT TDE model parameters. Units are listed where appropriate. The listed uncertainties include both statistical uncertainties from the fit and the systematic uncertainties listed in Table 3 of Mockler et al. (2019).

(2019). Finally, MOSFiT indicates that the star was likely completely disrupted in the encounter, though the lower limit on the scaled β parameter b is consistent with a partial disruption when the systematic uncertainties are taken into account.

3.2 Spectra

The early-time spectra of ASASSN-19dj have the very blue continuum that is a hallmark of tidal disruption events. This excess in blue flux grows towards peak light and fades back to host galaxy levels at later times. The very early-time optical spectra of ASASSN-19dj lack many of the spectral features that TDEs usually exhibit. For example, in the earliest spectrum, taken approximately 17 days after first light (see §3.1), the spectrum does not have strong broad H and He lines. Looking at Figure 8, which zooms into a small region around $H\alpha$, we see that the $H\alpha$ line slowly grows in strength from $\text{MJD} \approx 58539$ to $\text{MJD} \approx 58544$, and quickly becomes very strong by $\text{MJD} \approx 58571$, with a peak line flux of $\sim 2.5 \times 10^{-13} \text{erg cm}^{-2} \text{s}^{-1}$ or a luminosity of $\sim 2.9 \times 10^{41} \text{erg s}^{-1}$ at the distance of ASASSN-19dj. The line remains at roughly the same strength until at least 41 days later, after which the source became Sun-constrained. After the seasonal gap, we find evidence for weak $H\alpha$ emission as late as ~ 260 days after peak, consistent with other optical TDEs (e.g., Hung et al. 2020; Holoien et al. 2020). Figure 9 shows the luminosity and FWHM evolution of $H\alpha$ as a function of time and the luminosity versus line width. The line width increases towards peak line flux and decreases thereafter, with some epochs exhibiting very broad $H\alpha$, up to roughly $3 \times 10^4 \text{km s}^{-1}$. The positive correlation seen here between $H\alpha$ line flux and line width agrees with what has been observed in the TDEs PS18kh (Hung et al. 2019; Holoien et al. 2019b), ASASSN-18pg (Leloudas et al. 2019; Holoien et al. 2020), and ASASSN-18ul (Wevers et al. 2019b). Unlike other TDEs such as ASASSN-18pg (Holoien et al. 2020), we do not see evidence for both a broad and narrow component of the $H\alpha$ emission. While the dominant spectral features of ASASSN-19dj appear to be broad hydrogen lines, van Velzen et al. (2020) classify ASASSN-19dj as a TDE-Bowen object.

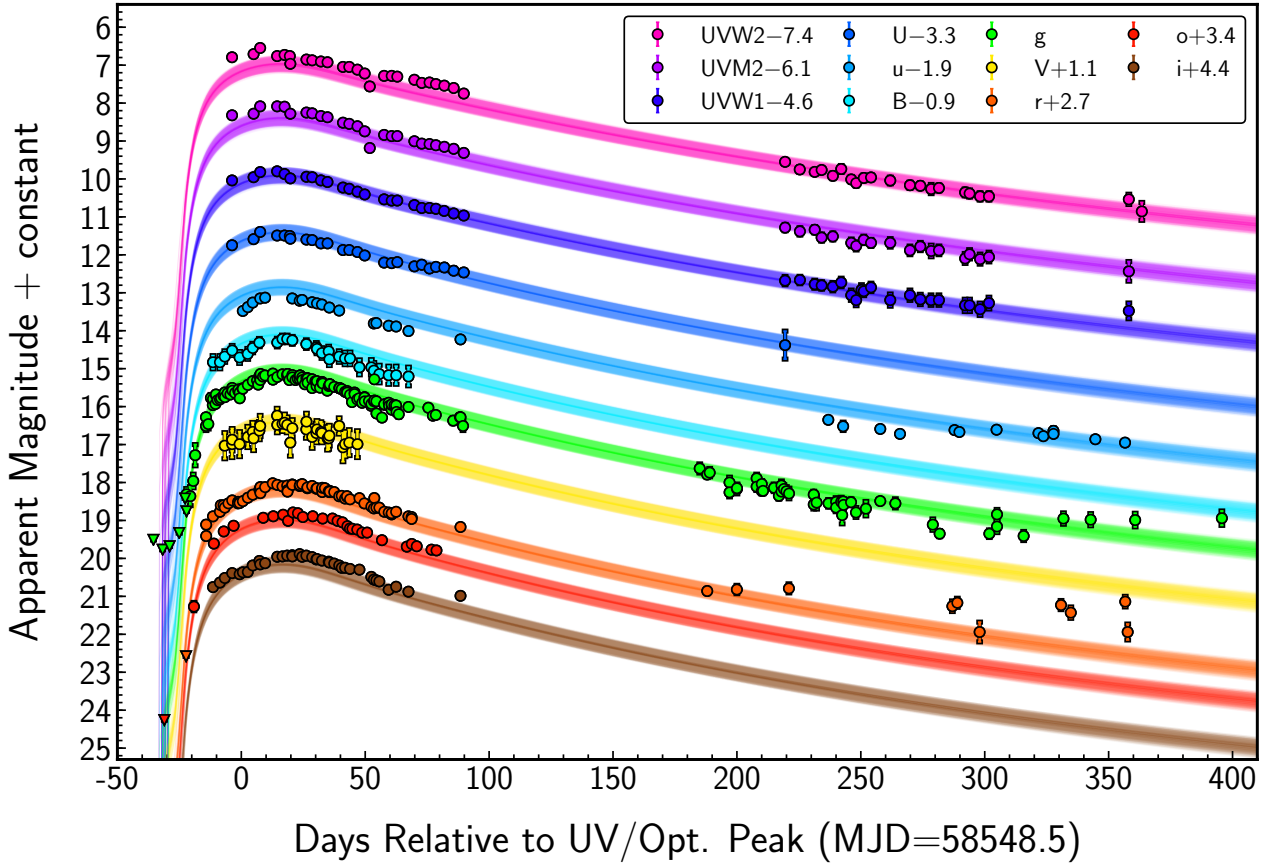


Figure 7. MOSFiT light curve fits and host-subtracted light curves. The the 1 – 99% range of fits for each filter are shown as shaded regions with the median fit shown as a solid line. All detections are plotted as circles with 3σ upper limits plotted as downward triangles. The colours match those of Figure 4.

Accordingly, there may be some evidence for broad emission centered on $\sim 4600 \text{ \AA}$, although the origin of this feature is difficult to determine.

Throughout the evolution of ASASSN-19dj, the $H\alpha$ line is very broad. There may be weak evidence for a broadening of the $H\alpha$ line at early times, similar to PS18kh (Holoien et al. 2019a), although we note these epochs have large uncertainties on the FWHM. The $H\alpha$ line begins to narrow again after the peak $H\alpha$ luminosity. There is a time delay between the peak UV/optical magnitude, which occurs at $\text{MJD} = 58545.5$, and the peak $H\alpha$ luminosity, at roughly $\text{MJD} \approx 58571$. As can be seen in Figure 9, the $H\alpha$ luminosity tracks the bolometric luminosity reasonably well when offset by 25 days. While this delay of ~ 25 days is only approximate, given our lack of spectra near this time, this provides an upper-limit on how far from the SMBH this emission is located. If the lines are due to reprocessing of high-energy FUV and X-ray photons produced in an accretion disk, this suggests the existence of reprocessing material at a distance of several tens of thousands of gravitational radii, slightly larger than the distance to reprocessing material derived for ASASSN-18pg, which also showed clear evidence for a delay between the bolometric peak and peak line emission (Holoien et al. 2020).

3.3 Spectral Energy Distribution

Figure 10 shows the blackbody model fits in terms of luminosity, radius, and temperature for ASASSN-19dj. ASASSN-19dj is one of the most luminous TDEs discovered to date, with a peak luminosity of $(6.15 \pm 0.17) \times 10^{44} \text{ erg s}^{-1}$, consistent with the value derived by Liu et al. (2019). This peak luminosity is comparable only to the TDE ASASSN-18ul (Wevers et al. 2019b, Payne et al. in preparation) and the TDE/AGN ASASSN-18jd (Neustadt et al. 2019). The decline in bolometric luminosity of ASASSN-19dj is quite slow, which is consistent with the findings of Hinkle et al. (2020) that more luminous TDEs decay slower than less luminous TDEs. At later times (over ~ 250 days after peak) the luminosity appears to flatten out, consistent with other TDEs with late-time observations including ASASSN-14li (Brown et al. 2017), ASASSN-15oi (Holoien et al. 2016a), ASASSN-18pg (Leloudas et al. 2019; Holoien et al. 2020), ASASSN-18ul (Wevers et al. 2019b, Payne et al. in preparation), and ATLAS18way (van Velzen et al. 2020). In the cases of both ASASSN-19dj and ASASSN-15oi (Gezari et al. 2017; Holoien et al. 2018), the flattening of the bolometric light curve is roughly coincident with and increase in X-ray flux.

The blackbody radius of ASASSN-19dj is initially relatively small compared to other well-studied TDEs with similar strong $H\alpha$ emission such as ASASSN-18zj (Hung

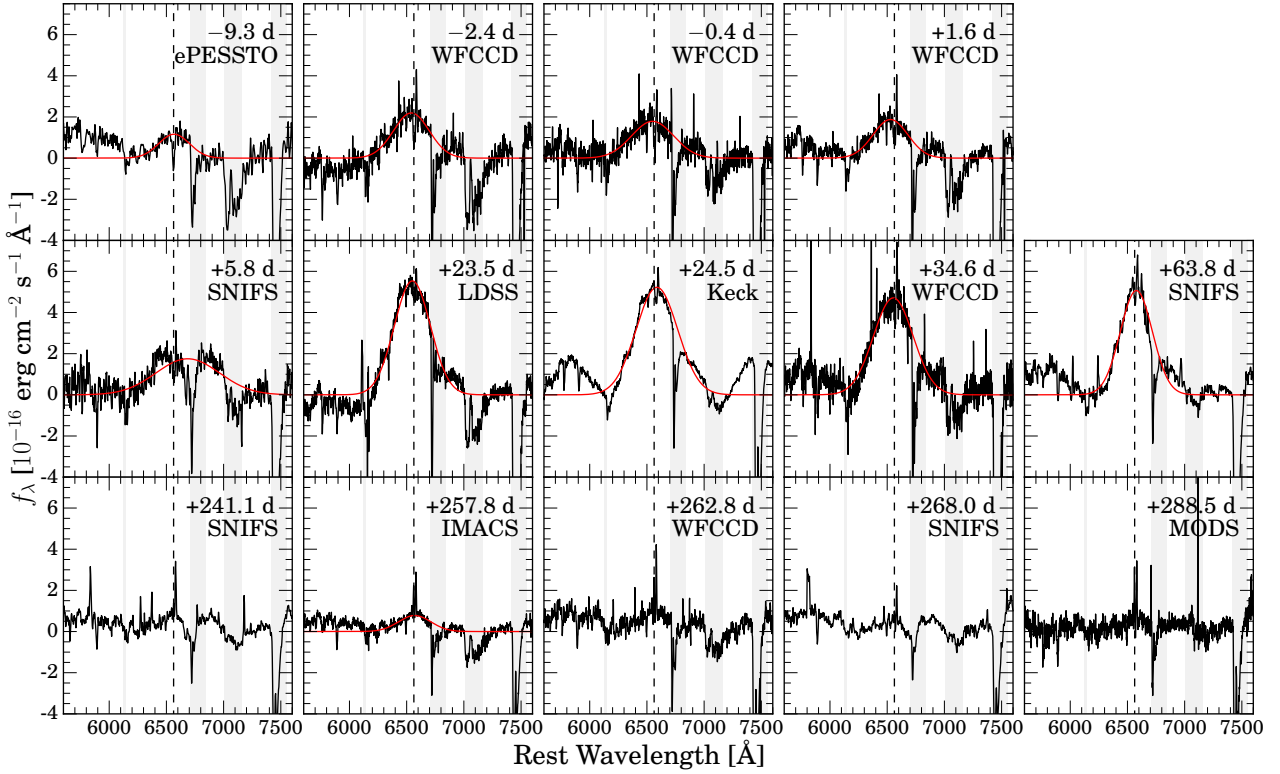


Figure 8. Spectral evolution of the $H\alpha$ line, increasing in time from top left to bottom right. The days relative to peak (MJD = 58548.5) in observer-frame days, of that particular spectral epoch and the instrument used to take the spectrum are shown in each individual panel. The red solid lines are Gaussian fits to the $H\alpha$ line profile, and are only shown for epochs with evidence of line emission. The vertical gray bands mark atmospheric telluric features.

et al. 2020; Short et al. 2020), ASASSN-19bt (Holoien et al. 2019b), and PS18kh (Holoien et al. 2019a) as well as the TDE/AGN ASASSN-18jd (Neustadt et al. 2019). It is larger however than other X-ray bright TDEs like ASASSN-14li (Holoien et al. 2016b; Brown et al. 2017) and ASASSN-15oi (Holoien et al. 2016a). At late times the radius continues to decrease slowly, becoming consistent with other TDEs with well-sampled late-time evolution such as ASASSN-14li (Holoien et al. 2016b) and ASASSN-15oi (Holoien et al. 2018). Additionally this slow late-time decrease in radius is consistent with many TDEs in the literature (e.g., van Velzen et al. 2020; Hinkle et al. 2020).

Unlike other TDEs with strong $H\alpha$ emission (ASASSN-18zj, ASASSN-19bt, and PS18kh) and the TDE/AGN ASASSN-18jd, the temperature of ASASSN-19dj is quite hot, on the order of ~ 45000 K. This temperature is more in line with the TDE-Bowen spectral class introduced by van Velzen et al. (2020), although we do not see strong evidence for Bowen fluorescence emission. This hot temperature, especially at late times, is similar to the TDEs ASASSN-18pg, ASASSN-15oi, ASASSN-14li, with the latter two also exhibiting late time X-ray emission. The blackbody temperatures of each of these TDEs are mostly flat throughout the evolution of the TDE. The blackbody temperature of ASASSN-19dj appears to decrease near peak, which can also be seen in Figure 4 as the time of peak is earliest in the bluest bands and delayed in each of the red bands, similar to other TDEs with high-cadence pre-peak photometry such

as ASASSN-19bt (Holoien et al. 2019b) and ASASSN-18pg (Holoien et al. 2020).

The UV/optical and X-ray SEDs at four epochs in the evolution of ASASSN-19dj are shown in Figure 11. The UV/optical emission of ASASSN-19dj is dominant at early times and several orders of magnitude brighter than the X-ray emission. Using the SMBH mass derived from MOSFiT, we calculate an Eddington luminosity of 9.8×10^{44} erg s $^{-1}$. Similar to what we find from the X-ray properties, we find no evidence for a plateau caused by Eddington-limited accretion near peak in either the bolometric light curve (see Fig. 10) or the single-band UV and optical light curves (see Fig. 4). The Eddington ratio for the peak bolometric luminosity is ~ 0.6 , which is consistent with other UV/optical TDEs in the literature (e.g., Wevers et al. 2017; Mockler et al. 2019). By roughly 250 days after peak, the X-ray emission exceeded the UV/optical emission by roughly an order of magnitude, similar to the late-time X-ray brightening of ASASSN-15oi (Gezari et al. 2017; Holoien et al. 2018) and ASASSN-19dj (Liu et al. 2019), as well as the flatter late-time X-ray emission of ASASSN-14li (Brown et al. 2017). During the epoch of peak X-ray emission, at MJD ≈ 58782 , the difference between the UV/optical and X-ray SEDs is less pronounced. By roughly a year after peak, both the X-ray and UV/optical SEDs have faded and are comparable in peak luminosity.

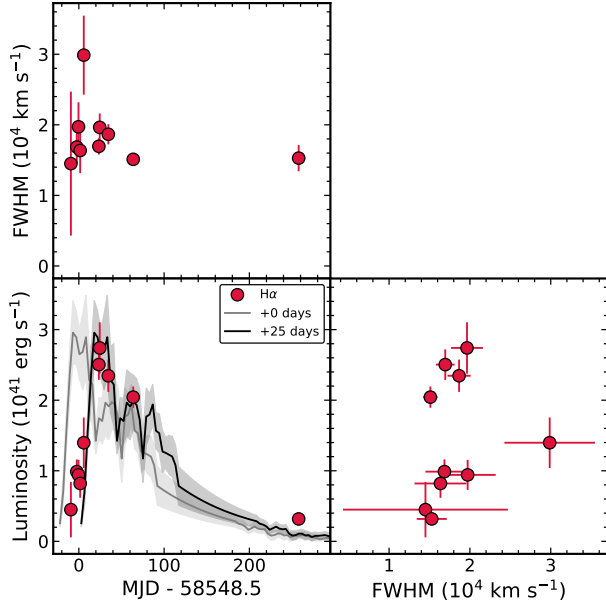


Figure 9. *Top Left Panel:* H α FWHM as a function of time. *Bottom Left Panel:* Time evolution of H α luminosity (red points). The bolometric light curve is scaled by a factor of 4.5×10^{-4} and shown with shaded error bars at zero days offset (gray) and 25 days offset (black) to highlight the delay in bolometric and H α peak. The bolometric light curves are smoothed by linearly interpolating to a time-series with the same length as the original coverage, but with half the number of points. *Right Panel:* H α luminosity as compared to the FWHM of the line.

3.4 Pre-ASASSN-19dj Outburst?

The CRTS light curve of the host galaxy, KUG 0810+227, shows evidence of a previous outburst in September 2005 (see Figure 3), roughly 14.5 years prior to this TDE. The data quality of the archival CRTS images of the host galaxy were too poor to perform image subtraction. Instead, we stacked six CRTS images of the host galaxy during the outburst and seventeen reference images taken at least five years after the outburst. Through comparison of the image centroids for these stacks, we find the difference to be $0''.18 \pm 0''.32$, corresponding to a physical distance of 84 ± 152 pc. Given the low quality of the archival images, this uncertainty is estimated by taking the standard deviation of the centroids of each of the individual images. While this constraint on the location of this previous transient is based on unsubtracted images, and therefore includes host light, it appears to be consistent with the host nucleus. However, we can make several statistical statements based on previous analysis presented in this paper.

The absolute magnitude of the brightest CRTS epoch is $V = -19.1$ or $L_V = 1.4 \times 10^{43} \text{ erg s}^{-1}$ (corrected for Galactic extinction, but assuming no host galaxy reddening), which is more luminous than the observed magnitudes of many types of supernovae, but consistent with the absolute magnitudes of Type Ia supernovae (Folatelli et al. 2010; Richardson et al. 2014, e.g.). We attempted to fit the CRTS light curve of the archival outburst with SNooPy (Burns et al. 2011) to constrain the properties of the light curve. We used the default E(B-V) model, but assumed no host galaxy reddening given the single filter light curve. These fits get their shape infor-

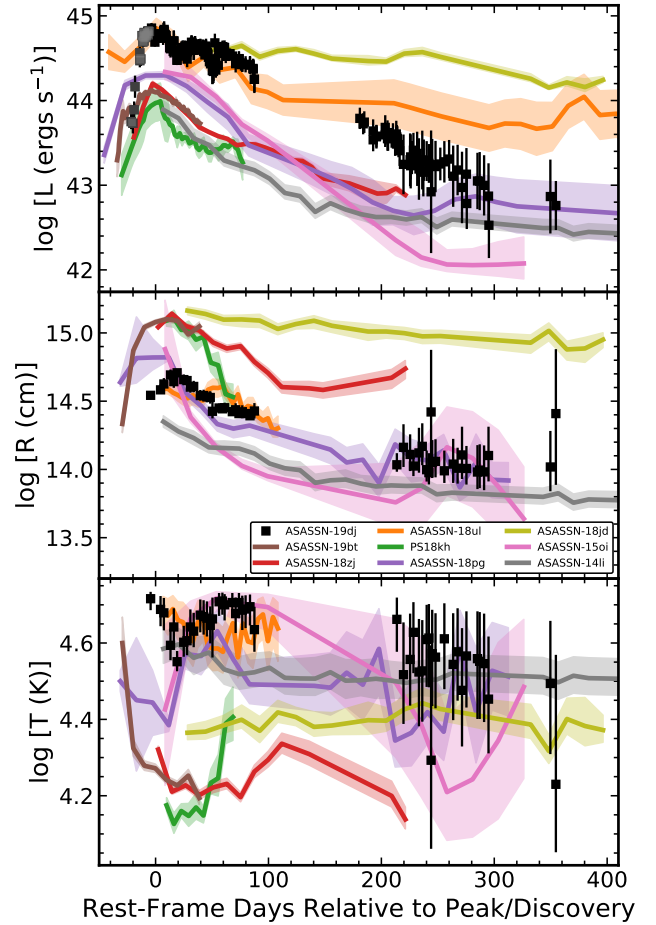


Figure 10. Evolution of the UV/optical blackbody luminosity (top panel), radius (middle panel), and temperature (bottom panel) for ASASSN-19dj (black squares), in comparison to other TDEs with strong H α emission, strong X-ray emission, or both: ASASSN-19bt (brown line; Holoien et al. 2019b), ASASSN-18zj (red line; van Velzen et al. 2020), ASASSN-18ul (orange line; Wevers et al. 2019b, Payne et al., in preparation), PS18kh (green line; Holoien et al. 2019a), ASASSN-18pg (purple line; Holoien et al. 2020), ASASSN-15oi (pink line; Holoien et al. 2018), and ASASSN-14li (gray line; Brown et al. 2017) in addition to the TDE/AGN ASASSN-18jd (gold line; Neustadt et al. 2019). The lines are smoothed over the individual epochs by linearly interpolating to a time-series with the same length as the original coverage, but with half the number of points. Time is in rest-frame days relative to the peak luminosity for the objects discovered prior to peak (ASASSN-19dj, ASASSN-19bt, ASASSN-18zj, ASASSN-18ul, PS18kh, and ASASSN-18pg), and relative to discovery for those which were not (ASASSN-18jd, ASASSN-15oi, and ASASSN-14li). The gray squares for ASASSN-19dj indicate where data has been bolometrically corrected using the ASASSN g-band light curve assuming the temperature from the first *Swift* epoch was constant.

mation from the fitted Δm_{15} and use the K-corrections of Hsiao et al. (2007), the Milky Way dust map of Schlegel et al. (1998), and SN templates of Prieto et al. (2006). From this, we find that the decline of this outburst is somewhat slower than expected for a Type Ia supernova, with $\Delta m_{15} = 0.8 \pm 0.4$ mag. Yet, given the data quality and maximum observed V-

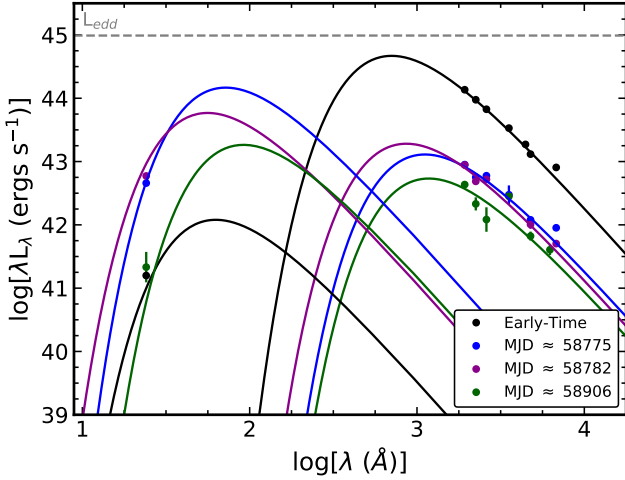


Figure 11. Spectral energy distribution of ASASSN-19dj at four different epochs. The first epoch (black) is at MJD = 58544 for the UV/optical emission and is the stacked early-time *Swift* for the X-ray. The second epoch (blue) is the first epoch after the X-ray brightening at MJD \approx 58775 for both the UV/optical and X-ray. The third epoch (purple) is the epoch of peak X-ray emission at MJD \approx 58782. The fourth epoch (green) is a late-time epoch at MJD \approx 58906. For each epoch, the data is shown as points while the lines represent the best fit blackbody components for the UV/optical and X-ray emission. The dashed gray line indicates the Eddington luminosity for an SMBH of mass $7.8 \times 10^6 M_\odot$, the SMBH mass derived from MOSFiT.

band magnitude, we cannot rule out a luminous Type Ia SN. We note that the true peak luminosity of this transient is likely higher than $1.4 \times 10^{43} \text{ erg s}^{-1}$, because a seasonal gap occurred immediately prior to the CRTS detection. Even if the peak luminosity is higher than this it may still be consistent with the tail of observed SN Ia magnitudes (e.g., Follatelli et al. 2010; Richardson et al. 2014) or a superluminous supernova.

Next, we evaluated the possibility that this CRTS flare was a previous TDE, by estimating a TDE rate for the host galaxy. The rate of TDEs is roughly $10^{-4} - 10^{-5} \text{ yr}^{-1}$ per galaxy (e.g., van Velzen & Farrar 2014; Holoien et al. 2016b; Auchettl et al. 2018) for an average galaxy. However, KUG 0810+227 is a post-starburst galaxy, for which it is known that the TDE rate can be enhanced by up to 200 times the average (e.g., French et al. 2016; Law-Smith et al. 2017; Graur et al. 2018), and thus it would not be unreasonable that a TDE could occur every 50 - 500 years. Even within this sample of post-starburst galaxies, KUG 0810+227 appears to be extreme in terms of its Lick $H\delta_A$ index. Counting galaxies with $H\delta_A - \sigma(H\delta_A) > 7.0 \text{ \AA}$ and $H\alpha$ emission EW $< 3.0 \text{ \AA}$, gives just 0.025% of all the galaxies in SDSS and a similar TDE rate enhancement of ~ 250 times the average. Thus, there is the possibility that the CRTS flare is a previous TDE.

Several pieces of archival data and optical emission line diagnostics are consistent with KUG 0810+227 being a LLAGN. The line ratios of the optical spectrum of KUG 0810+227 lie in the LINER region of two line ratio diagnostic diagrams, which suggests the possibility of the host being a LLAGN. However, we note that the WHAN diagram clas-

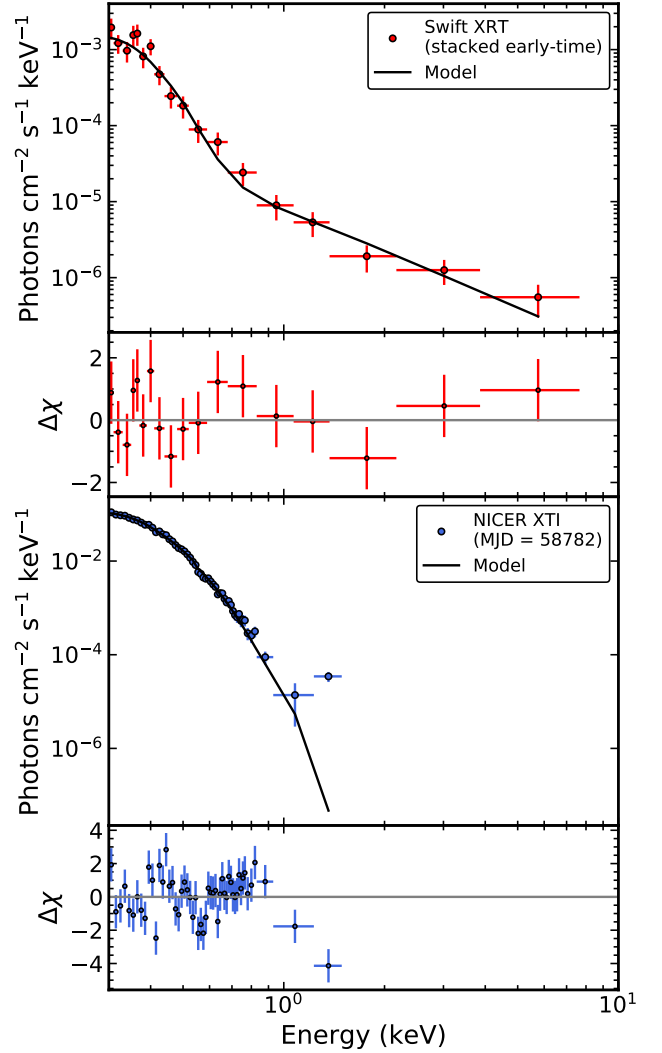


Figure 12. X-ray spectrum and $\Delta\chi$ for the stacked early-time *Swift* observations (top panel) and *NICER* observations of ASASSN-19dj at peak X-ray emission on MJD = 58782 (bottom panel). The black lines in the top and bottom panels are the best-fit absorbed blackbody model + power-law and absorbed blackbody models respectively. The reduced χ^2 of the best-fit models are 0.90 for 15 degrees of freedom and 1.72 for 50 degrees of freedom respectively.

sifies KUG 0810+227 as an RG, suggesting a possible non-AGN ionization source. In the X-ray, the first *Swift* XRT epoch gives a deep upper limit, which is consistent with a small fraction of observed X-ray luminosities of AGN (e.g., Tozzi et al. 2006; Ricci et al. 2017). Therefore, because the host is consistent with a LLAGN, the previous flare could be associated with a pre-flare AGN outburst.

3.5 X-rays

ASASSN-19dj is one of several optical TDEs to show strong X-ray emission. In Figure 12, we show the stacked early-time *Swift* spectrum and a *NICER* spectrum from the epoch of peak X-ray emission. In Figure 13 (top panel), we show the X-ray light curve as derived from both the individual

Table 5. X-ray spectral parameters of ASASSN-19dj

| MJD | N_H (10^{20} cm $^{-2}$) | N_H Error (10^{20} cm $^{-2}$) | kT (keV) | kT Error (keV) | log Radius (cm) | Radius Error (cm) | Satellite |
|-------------------|-----------------------------------|---|-------------|-------------------|--------------------|----------------------|--------------|
| 58544.75-58638.27 | 4.06 | 4.00 | 0.050 | 0.009 | 11.15 | 0.38 | <i>Swift</i> |
| 58767.93-58779.88 | 7.55 | 5.00 | 0.048 | 0.010 | 12.12 | 0.42 | <i>Swift</i> |
| 58782.67 | 3.98 | 3.00 | 0.062 | 0.005 | 11.69 | 0.29 | <i>Swift</i> |
| ... | ... | ... | ... | ... | ... | ... | ... |
| 58920.19 | 4.16 | — | 0.035 | 0.002 | 12.22 | 0.27 | <i>NICER</i> |
| 58934.02 | 4.16 | — | 0.030 | 0.002 | 12.54 | 0.33 | <i>NICER</i> |
| 58940.53 | 4.16 | — | 0.028 | 0.002 | 12.59 | 0.34 | <i>NICER</i> |

Neutral hydrogen column densities, blackbody temperatures, and effect blackbody radii derived from the various X-ray spectral epoch. A range of MJD in the first column indicates the beginning and end of the range over which data were stacked to increase S/N. The last column reports the source of the data for each epoch. Only a small section of the table is displayed here. The full table can be found online as an ancillary file.

Swift and *NICER* observations. To estimate the X-ray luminosity, we converted the extracted count rate into flux using WebPIMMS¹¹ and assumed an absorbed blackbody model with a temperature of ~ 50 eV, corresponding to the average blackbody temperature derived from our *Swift* and *NICER* X-ray spectra. This value is also consistent with the blackbody temperatures of other X-ray bright TDEs (e.g., ASASSN-14li, ASASSN-15oi [Brown et al. 2017](#); [Holoien et al. 2018](#); [Kara et al. 2018a](#)). The first X-ray observation of ASASSN-19dj was taken using the *Swift* XRT approximately 4 days before the peak UV/optical emission (MJD = 58544.8). During this observation, ASASSN-19dj showed no evidence of X-ray emission with a 3σ upper limit of 6×10^{40} erg s $^{-1}$, consistent with the limits/detection of X-ray emission seen prior to peak in the TDEs ASASSN-19bt ([Holoien et al. 2019b](#)), ASASSN-18pg ([Leloudas et al. 2019](#); [Holoien et al. 2020](#)), AT2019qiz ([Auchettl et al. 2019](#)) and other X-ray TDE candidates ([Auchettl et al. 2017](#)). We note that this upper limit places even stricter constraints on the possibility that the host galaxy is a LLAGN, with [Tozzi et al. \(2006\)](#) finding that fewer than $\sim 10\%$ of AGN have X-ray luminosities this low, and [Ricci et al. \(2017\)](#) measuring only 1% of their unobscured non-blazar AGN sample to have X-ray luminosities this low.

ASASSN-19dj was first detected in X-rays ~ 9 days later, ~ 4 days after the UV/optical peak, in the second *Swift* XRT observation, with its X-ray luminosity increasing by at least half an order of magnitude to $\sim 3 \times 10^{41}$ erg s $^{-1}$. Similar to ASASSN-18jd ([Neustadt et al. 2019](#)), ASASSN-18ul ([Wevers et al. 2019b](#)) and ASASSN-15oi ([Gezari et al. 2017](#)), the X-ray emission of ASASSN-19dj showed significant variations in luminosity over the first ~ 100 days after peak, varying between $\sim 10^{40.7} - 10^{41.7}$ erg s $^{-1}$ before the seasonal gap, much larger than the variability seen in ASASSN-14li ([Brown et al. 2017](#)), but similar to that seen in ASASSN-18jd ([Neustadt et al. 2019](#)) or ASASSN-18ul ([Wevers et al. 2019b](#)). Once the source became visible again ~ 220 days after peak, *XMM-Newton* slew, *Swift* XRT, and *NICER* observations found that the source had brightened by nearly a factor of ~ 10 . This brightening behaviour is reminiscent of

what was seen in ASASSN-15oi ([Gezari et al. 2017](#); [Holoien et al. 2018](#)) and hinted at in ASASSN-18ul ([Wevers et al. 2019b](#)), in which the X-ray emission increased by an order of magnitude ~ 250 days after peak brightness before fading. ASASSN-19dj peaked at an X-ray luminosity of $\sim 10^{43}$ erg s $^{-1}$ before fading by nearly an order of magnitude over ~ 100 days and then plateauing at an X-ray luminosity of $\sim 10^{42}$ erg s $^{-1}$. The peak luminosity corresponds an Eddington ratio between 0.01-0.03, consistent with other X-ray bright TDEs ([Mockler et al. 2019](#); [Wevers et al. 2019a](#)) and again disfavoring Eddington-limited accretion as suggested by [van Velzen et al. \(2019\)](#).

In Figure 13 (second panel), we present the evolution of the X-ray hardness ratio¹² (HR) as a function of time. At early times, ASASSN-19dj shows significant variability in its hardness, varying between a soft HR of -1 and harder HR of -0.2 during the first 100 days. By 200-280 after days after peak, the hardness ratio of ASASSN-19dj plateaued to a soft HR between -1 and -0.8 , before hardened significantly over ~ 20 days from 280-300 days after peak. Finally, from 300 days after peak onwards, ASASSN-19dj returned to the HR variability observed at early times. The behaviour seen at early times is consistent with the presence of hard X-ray emission in the form of a power-law in addition to a soft thermal blackbody, consistent with [Liu et al. \(2019\)](#). This can be seen in the merged *Swift* spectra derived from the observations taken within the first 100 days (see Fig. 12). The softening of the X-ray emission between 200 to ~ 280 days after discovery occurs when the X-ray emission from this event becomes dominated by a strong thermal blackbody component. Near peak, the constant HR with time and decreasing X-ray luminosity, is consistent with that exhibited by non-thermal TDEs such as ASASSN-14li ([Auchettl et al. 2018](#)). However, we note that the lack of significant HR evolution seen in ASASSN-14li begins at peak brightness in X-ray, UV/optical and bolometric luminosity and continues for thousands of days after peak. As the blackbody component cools with time and fades, the X-ray emission is seen to harden, similar to what was seen in ASASSN-14li (e.g., [Kara et al. 2018b](#)).

¹¹ <https://heasarc.gsfc.nasa.gov/cgi-bin/Tools/w3pimms/w3pimms.pl>

¹² The hardness ratio (HR) is defined as $HR = (H-S)/(H+S)$ where H is the number of counts in the 2.0-10.0 keV energy range and S is the number of counts in the 0.3-2.0 keV energy range

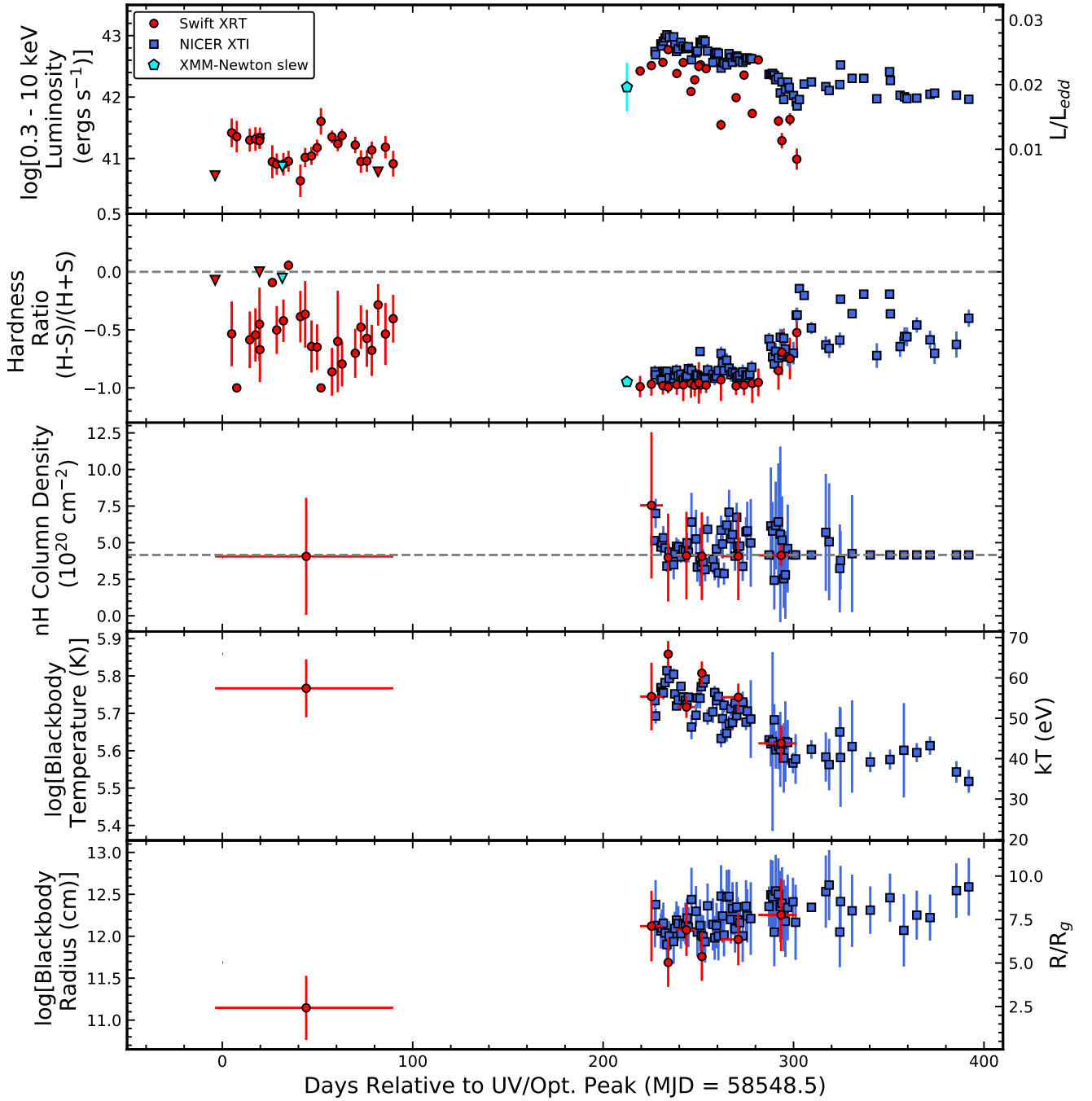


Figure 13. In order from top to bottom: X-ray luminosity, hardness ratio, neutral hydrogen column density (with the dashed gray line marking the Galactic column density), blackbody radius, and blackbody temperature of ASASSN-19dj measured with *Swift* (red circles), *NICER* (blue squares) and *XMM-Newton* slew (cyan pentagon). We define hard counts H as the number of counts in the 2-10 keV range and soft counts S are the number of counts in the 0.3-2 keV range, with a gray dashed line marking zero. The hardness ratio is defined as $(H-S)/(H+S)$. Downward-facing triangles mark upper limits.

During the evolution of ASASSN-19dj, the HR and the X-ray luminosity seem to follow an inverse relationship, where the X-ray emission becomes harder as the luminosity of the source fades, and becomes softer as the source brightens. This relationship is shown in Figure 14, with colour-coding and arrows to highlight the trend. This evolution is consistent with what is seen in highly variable, X-ray bright

AGN (c.f. Figure 4 of [Auchettl et al. 2018](#)). The overall behaviour seen in ASASSN-19dj is quite unique compared to all other X-ray TDE candidates, even compared to ASASSN-15oi, which showed delayed brightening of the X-ray emission ~ 200 after peak UV brightness ([Gezari et al. 2017](#)), or ASASSN-18jd which showed large variations in HR with time before the emission completely faded ([Neustadt et al.](#)

2019). Auchettl et al. (2018) showed that <4% of X-ray bright AGN could produce flare emission that exhibits a coherent decay and a constant HR similar to that of an X-ray bright TDE. So while the brightening is similar to what we see from thermal TDEs such as ASASSN-14li, we cannot rule out that some of the emission arises from a pre-existing AGN disk (e.g., Blanchard et al. 2017).

To further explore the nature of the X-ray emission arising from ASASSN-19dj, we analysed the *Swift* and *NICER* spectra using the X-ray spectral fitting program XSPEC version 12.10.1f (Arnaud 1996), and chi-squared statistics. While we fit the majority of *NICER* spectra individually (with the exception of a handful of observations at late times), it was necessary to stack the early-time *Swift* observations to get adequate S/N. We show the results of these spectral fits in the bottom three panels of Figure 13.

At early times, the merged *Swift* spectrum is best fit by an absorbed blackbody plus power-law model. However, at late times, when ASASSN-19dj is significantly brighter, we find that an absorbed blackbody is sufficient to model the observed spectra. We let the column density (N_H), blackbody temperature (kT) and blackbody normalisation, as well as the photon-index Γ and powerlaw normalisation for the early *Swift* spectra, of each model be free parameters. In Table 5 we summarise the best-fit parameters of our spectral fits.

The third panel of Figure 13 shows the column density as a function of time. We find that due to the large uncertainties the column density derived using the *NICER* spectra and merged *Swift* spectra is consistent with the Galactic column density along the line of sight.

In Figure 13 (fourth panel), we show the temperature evolution of ASASSN-19dj. We find that the derived X-ray blackbody temperatures are similar to other X-ray bright TDEs such as ASASSN-14li (Holoien et al. 2016b; Brown et al. 2017) and ASASSN-15oi (Gezari et al. 2017; Holoien et al. 2018), and the very tail end of the blackbody temperature distribution of unobserved non-blazar AGN (Ricci et al. 2017), peaking at $kT \sim 110$ eV. We find that the temperature of ASASSN-19dj is lower than derived for the TDE/AGN candidates ASASSN-18jd Neustadt et al. (2019) and ASASSN-18ul (Wevers et al. 2019b) which had blackbody temperatures more consistent with known AGN. Initially, we find that the blackbody component had a mean temperature of ~ 60 eV. Unfortunately, due to the faintness of the source at early times, we are unable to constrain whether the temperature is constant with time or varies as seen during the late phases of its evolution. Interestingly, when the luminosity of the source increases after the seasonal gap, we find that the temperature initially does not change significantly from that seen at early times. However, as the source increases to peak brightness, we find that the temperature also increases, peaking at 62 ± 5 eV. As the source begins to fade, the temperature seems to follow the same short timescale variability behaviour seen in the X-ray light curve, suggesting that the short time scale luminosity variation we observe is dominated by changes in the blackbody temperature with time. The change in temperature is most dramatic between 200–280 days after the peak of the UV/optical light curve, where the blackbody temperature drops from ~ 60 keV to ~ 40 keV, before plateauing at this lower temperature value for the next ~ 100 days, similar to

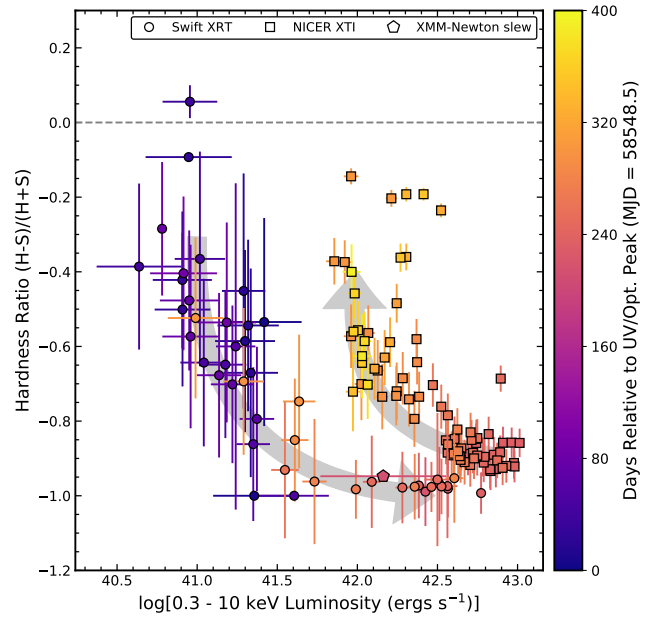


Figure 14. Hardness ratio as a function of X-ray luminosity as measured by *Swift* (red circles), *NICER* (blue squares), and *XMM-Newton* slew (cyan pentagon) for the detections only. Light gray arrows indicate that as ASASSN-19dj becomes brighter, the X-ray emission becomes softer. This behaviour is similar to that seen in X-ray bright AGN (Auchettl et al. 2018). The colour bar on the right indicates the phase relative to the UV/optical peak, with darker colours indicating earlier times.

what was seen in ASASSN-14li after peak X-ray brightness (see Table 3 of Brown et al. 2017).

In the bottom panel of Figure 13 we show the evolution of the effective blackbody radius as a function of time. During its early evolution ASASSN-19dj has a blackbody radius that is consistent with ASASSN-18jd (Neustadt et al. 2019) and ASASSN-15oi (Holoien et al. 2018) both before and after its observed X-ray brightening. The brightening of ASASSN-19dj after the seasonal gap is also associated with a dramatic order of magnitude increase in the blackbody radius. This suggests that the increase in X-ray luminosity is a result of an expansion of the X-ray emitting region rather than delayed accretion that could result from inefficient circularisation as suggested for ASASSN-15oi (Gezari et al. 2017) and for ASASSN-19dj (Liu et al. 2019). van Velzen et al. (2020) also find that the X-ray brightening of ASASSN-19dj does not require delayed accretion. The size of the blackbody radius of ASASSN-19dj is consistent with ASASSN-14li (Brown et al. 2017), ASASSN-15oi (Holoien et al. 2018), and other TDE candidates whose blackbody radii were measured at peak using X-rays (see Figure 11 of Wevers et al. 2019a).

Similar to Wevers et al. (2019a) and individual studies of X-ray bright TDE candidates (e.g., Brown et al. 2017; Holoien et al. 2018), we find that the X-ray emitting region is at least an order of magnitude smaller than the blackbody radius interfered from the UV/optical (see Figure 10). Additionally, the blackbody radius is smaller than (at early times) and equal to (at peak brightness) the ISCO (innermost stable circular orbit) of the black hole, assuming a Schwarzschild

stitute for Extraterrestrial Physics, Garching, The Johns Hopkins University, Durham University, the University of Edinburgh, the Queen's University Belfast, the Harvard-Smithsonian Center for Astrophysics, the Las Cumbres Observatory Global Telescope Network Incorporated, the National Central University of Taiwan, the Space Telescope Science Institute, the National Aeronautics and Space Administration under Grant No. NNX08AR22G issued through the Planetary Science Division of the NASA Science Mission Directorate, the National Science Foundation Grant No. AST-1238877, the University of Maryland, Eotvos Lorand University (ELTE), the Los Alamos National Laboratory, and the Gordon and Betty Moore Foundation.

Support for ATLAS observations and data products was provided by NASA grant NN12AR55G and 80NSSC18K0284.

The CSS survey is funded by the National Aeronautics and Space Administration under Grant No. NNG05GF22G issued through the Science Mission Directorate Near-Earth Objects Observations Program. The CRTS survey is supported by the U.S. National Science Foundation under grants AST-0909182.

Some of the data presented herein were obtained at the W. M. Keck Observatory, which is operated as a scientific partnership among the California Institute of Technology, the University of California and the National Aeronautics and Space Administration. The Observatory was made possible by the generous financial support of the W. M. Keck Foundation.

The LBT is an international collaboration among institutions in the United States, Italy and Germany. LBT Corporation partners are: The University of Arizona on behalf of the Arizona Board of Regents; Istituto Nazionale di Astrofisica, Italy; LBT Beteiligungsgesellschaft, Germany, representing the Max-Planck Society, The Leibniz Institute for Astrophysics Potsdam, and Heidelberg University; The Ohio State University, and The Research Corporation, on behalf of The University of Notre Dame, University of Minnesota and University of Virginia.

This work is based on observations made by ASAS-SN, ATLAS, Pan-STARRS, UH88, and Keck. We wish to extend our special thanks to those of Hawaiian ancestry on whose sacred mountains of Maunakea and Haleakalā, we are privileged to be guests. Without their generous hospitality, the observations presented herein would not have been possible.

REFERENCES

- Adelman-McCarthy J. K., et al., 2006, *ApJS*, **162**, 38
- Aguado D. S., et al., 2019, *ApJS*, **240**, 23
- Alard C., 2000a, *A&AS*, **144**, 363
- Alard C., 2000b, *AAPS*, **144**, 363
- Alard C., Lupton R. H., 1998, *ApJ*, **503**, 325
- Arcavi I., et al., 2014, *ApJ*, **793**, 38
- Arnaud K. A., 1996, in Jacoby G. H., Barnes J., eds, *Astronomical Society of the Pacific Conference Series Vol. 101, Astronomical Data Analysis Software and Systems V*. p. 17
- Assef R. J., et al., 2013, *ApJ*, **772**, 26
- Atkinson J. W., et al., 2005, *MNRAS*, **359**, 504
- Auchettl K., Guillochon J., Ramirez-Ruiz E., 2017, *ApJ*, **838**, 149
- Auchettl K., Ramirez-Ruiz E., Guillochon J., 2018, *ApJ*, **852**, 37
- Auchettl K., Hung T., Foley R. J., Stanek K. Z., Kochanek C. S., Mathur S., Shappee B. J., Holoien T. W. S., 2019, *The Astronomer's Telegram*, **13143**, 1
- Bade N., Komossa S., Dahlem M., 1996, *A&A*, **309**, L35
- Baldwin J. A., Phillips M. M., Terlevich R., 1981, *PASP*, **93**, 5
- Barbarino C., Carracedo A. S., Tartaglia L., Yaron O., 2019, *Transient Name Server Classification Report*, **2019-287**, 1
- Barron J. T., Stumm C., Hogg D. W., Lang D., Roweis S., 2008, *AJ*, **135**, 414
- Becker A., 2015, *HOTPANTS: High Order Transform of PSF AND Template Subtraction* (ascl:1504.004)
- Bellm E. C., et al., 2019, *PASP*, **131**, 018002
- Bertin E., Arnouts S., 1996, *A&AS*, **117**, 393
- Biehl D., Boncioli D., Lunardini C., Winter W., 2018, *Scientific Reports*, **8**, 10828
- Blanchard P. K., et al., 2017, preprint, ([arXiv:1703.07816](https://arxiv.org/abs/1703.07816))
- Bloom J. S., et al., 2011, *Science*, **333**, 203
- Bogdanov S., et al., 2019, *ApJ*, **887**, L25
- Bonnerot C., Rossi E. M., Lodato G., 2017, *MNRAS*, **464**, 2816
- Breeveld A. A., et al., 2010, *MNRAS*, **406**, 1687
- Brimacombe J., et al., 2019, *The Astronomer's Telegram*, **12526**, 1
- Brinchmann J., Charlot S., White S. D. M., Tremonti C., Kauffmann G., Heckman T., Brinkmann J., 2004, *MNRAS*, **351**, 1151
- Brown T. M., et al., 2013, *PASP*, **125**, 1031
- Brown J. S., Shappee B. J., Holoien T. W.-S., Stanek K. Z., Kochanek C. S., Prieto J. L., 2016, *MNRAS*, **462**, 3993
- Brown J. S., Holoien T. W.-S., Auchettl K., Stanek K. Z., Kochanek C. S., Shappee B. J., Prieto J. L., Grupe D., 2017, *MNRAS*, **466**, 4904
- Brown J. S., et al., 2018, *MNRAS*, **473**, 1130
- Bruzual G., Charlot S., 2003, *MNRAS*, **344**, 1000
- Burns C. R., et al., 2011, *AJ*, **141**, 19
- Burrows D. N., et al., 2005, *SSR*, **120**, 165
- Burrows D. N., et al., 2011, *Nature*, **476**, 421
- Cardelli J. A., Clayton G. C., Mathis J. S., 1988, *ApJ*, **329**, L33
- Cenko S. B., et al., 2012a, *MNRAS*, **420**, 2684
- Cenko S. B., et al., 2012b, *ApJ*, **753**, 77
- Chambers K. C., et al., 2016, preprint, ([arXiv:1612.05560](https://arxiv.org/abs/1612.05560))
- Chornock R., et al., 2014, *ApJ*, **780**, 44
- Cid Fernandes R., Stasińska G., Mateus A., Vale Asari N., 2011, *MNRAS*, **413**, 1687
- Coughlin E. R., Nixon C. J., 2019, *ApJ*, **883**, L17
- Dai L., McKinney J. C., Miller M. C., 2015, *ApJ*, **812**, L39
- Dai L., McKinney J. C., Roth N., Ramirez-Ruiz E., Miller M. C., 2018, *ApJ*, **859**, L20
- De Propriis R., Melnick J., 2014, *MNRAS*, **439**, 2837
- Drake A. J., et al., 2009, *ApJ*, **696**, 870
- Dressler A., et al., 2011, *PASP*, **123**, 288
- Eisenstein D. J., et al., 2011, *AJ*, **142**, 72
- Evans C. R., Kochanek C. S., 1989, *ApJ*, **346**, L13
- Event Horizon Telescope Collaboration et al., 2019, *ApJ*, **875**, L1
- Farrar G. R., Piran T., 2014, arXiv e-prints, [p. arXiv:1411.0704](https://arxiv.org/abs/1411.0704)
- Folatelli G., et al., 2010, *AJ*, **139**, 120
- Ford H. C., et al., 1994, *ApJ*, **435**, L27
- French K. D., Arcavi I., Zabludoff A., 2016, *ApJ*, **818**, L21
- French K. D., Arcavi I., Zabludoff A., 2017, *ApJ*, **835**, 176
- French K. D., Yang Y., Zabludoff A. I., Tremonti C. A., 2018, *ApJ*, **862**, 2
- French K. D., Arcavi I., Zabludoff A. I., Stone N., Hiramatsu D., van Velzen S., McCully C., Jiang N., 2020, *ApJ*, **891**, 93
- Gafton E., Rosswog S., 2019, *MNRAS*, **487**, 4790
- Gallegos-Garcia M., Law-Smith J., Ramirez-Ruiz E., 2018, *ApJ*, **857**, 109
- Gaskell C. M., Rojas Lobos P. A., 2014, *MNRAS*, **438**, L36
- Gebhardt K., Adams J., Richstone D., Lauer T. R., Faber S. M., Gültekin K., Murphy J., Tremaine S., 2011, *ApJ*, **729**, 119

- Gehrels N., et al., 2004, *ApJ*, **611**, 1005
- Gendreau K. C., Arzoumanian Z., Okajima T., 2012, The Neutron star Interior Composition Explorer (NICER): an Explorer mission of opportunity for soft x-ray timing spectroscopy. p. 844313, doi:10.1117/12.926396
- Gezari S., et al., 2006, *ApJ*, **653**, L25
- Gezari S., et al., 2008, *ApJ*, **676**, 944
- Gezari S., et al., 2009, *ApJ*, **698**, 1367
- Gezari S., et al., 2012, *Nature*, **485**, 217
- Gezari S., Cenko S. B., Arcavi I., 2017, *ApJ*, **851**, L47
- Ghez A. M., Salim S., Hornstein S. D., Tanner A., Lu J. R., Morris M., Becklin E. E., Duchêne G., 2005, *ApJ*, **620**, 744
- Golightly E. C. A., Coughlin E. R., Nixon C. J., 2019, *ApJ*, **872**, 163
- Graham A. W., Erwin P., Caon N., Trujillo I., 2001, *ApJ*, **563**, L11
- Graur O., French K. D., Zahid H. J., Guillochon J., Mandel K. S., Auchettl K., Zabludoff A. I., 2018, *ApJ*, **853**, 39
- Groves B. A., Dopita M. A., Sutherland R. S., 2004, *ApJS*, **153**, 75
- Grupe D., Thomas H.-C., Leighly K. M., 1999, *A&A*, **350**, L31
- Guillochon J., Ramirez-Ruiz E., 2013, *ApJ*, **767**, 25
- Guillochon J., Ramirez-Ruiz E., 2015, *ApJ*, **809**, 166
- Guillochon J., Manukian H., Ramirez-Ruiz E., 2014, *ApJ*, **783**, 23
- Guillochon J., Nicholl M., Villar V. A., Mockler B., Narayan G., Mandel K. S., Berger E., Williams P. K. G., 2017a, MOSFiT: Modular Open-Source Fitter for Transients, Astrophysics Source Code Library (ascl:1710.006)
- Guillochon J., Parrent J., Kelley L. Z., Margutti R., 2017b, *ApJ*, **835**, 64
- Gültekin K., et al., 2009, *ApJ*, **698**, 198
- HI4PI Collaboration et al., 2016, *A&A*, **594**, A116
- Heikkilä T., et al., 2019, The Astronomer's Telegram, 12529, 1
- Henden A. A., Levine S., Terrell D., Welch D. L., 2015, in American Astronomical Society Meeting Abstracts #225. p. 336.16
- Hill J. M., Green R. F., Slagle J. H., 2006, The Large Binocular Telescope. p. 62670Y, doi:10.1117/12.669832
- Hinkle J. T., Holoien T. W. S., Shappee B. J., Auchettl K., Kochanek C. S., Stanek K. Z., Payne A. V., Thompson T. A., 2020, arXiv e-prints, p. arXiv:2001.08215
- Ho L. C., 2008, *ARA&A*, **46**, 475
- Holoien T. W.-S., et al., 2014a, *MNRAS*, **445**, 3263
- Holoien T. W.-S., et al., 2014b, *ApJ*, **785**, L35
- Holoien T. W.-S., et al., 2016a, *Acta Astron.*, **66**, 219
- Holoien T. W.-S., et al., 2016b, *MNRAS*, **455**, 2918
- Holoien T. W.-S., et al., 2016c, *MNRAS*, **463**, 3813
- Holoien T. W.-S., Brown J. S., Auchettl K., Kochanek C. S., Prieto J. L., Shappee B. J., Van Saders J., 2018, *MNRAS*, **480**, 5689
- Holoien T. W. S., et al., 2019a, *ApJ*, **880**, 120
- Holoien T. W. S., et al., 2019b, *ApJ*, **883**, 111
- Holoien T. W. S., et al., 2020, arXiv e-prints, p. arXiv:2003.13693
- Hsiao E. Y., Conley A., Howell D. A., Sullivan M., Pritchett C. J., Carlberg R. G., Nugent P. E., Phillips M. M., 2007, *ApJ*, **663**, 1187
- Hung T., et al., 2017, *ApJ*, **842**, 29
- Hung T., et al., 2019, arXiv e-prints,
- Hung T., et al., 2020, arXiv e-prints, p. arXiv:2003.09427
- Jiang Y.-F., Guillochon J., Loeb A., 2016, *ApJ*, **830**, 125
- Jones D. O., et al., 2019, Transient Name Server AstroNote, 148, 1
- Kara E., Dai L., Reynolds C. S., Kallman T., 2018a, *MNRAS*, **474**, 3593
- Kara E., Dai L., Reynolds C. S., Kallman T., 2018b, *MNRAS*, **474**, 3593
- Kauffmann G., et al., 2003, *MNRAS*, **346**, 1055
- Kelson D. D., et al., 2014, *ApJ*, **783**, 110
- Kewley L. J., Dopita M. A., Sutherland R. S., Heisler C. A., Trevena J., 2001, *ApJ*, **556**, 121
- Kewley L. J., Groves B., Kauffmann G., Heckman T., 2006, *MNRAS*, **372**, 961
- Kochanek C. S., 1994, *ApJ*, **422**, 508
- Kochanek C. S., 2016a, *MNRAS*, **458**, 127
- Kochanek C. S., 2016b, *MNRAS*, **461**, 371
- Kochanek C. S., et al., 2017, *PASP*, **129**, 104502
- Komossa S., 2015, *Journal of High Energy Astrophysics*, **7**, 148
- Komossa S., Bade N., 1999, *A&A*, **343**, 775
- Komossa S., Greiner J., 1999, *A&A*, **349**, L45
- Kormendy J., Ho L. C., 2013, *ARA&A*, **51**, 511
- Kormendy J., Richstone D., 1995, *ARA&A*, **33**, 581
- Kormendy J., et al., 1996, *ApJ*, **459**, L57
- Kriek M., van Dokkum P. G., Labbé I., Franx M., Illingworth G. D., Marchesini D., Quadri R. F., 2009, *ApJ*, **700**, 221
- Krolik J., Piran T., Svirski G., Cheng R. M., 2016, *ApJ*, **827**, 127
- Krolik J., Piran T., Ryu T., 2020, arXiv e-prints, p. arXiv:2001.03234
- Lacy J. H., Townes C. H., Hollenbach D. J., 1982, *ApJ*, **262**, 120
- Lang D., Hogg D. W., Mierle K., Blanton M., Roweis S., 2010, *AJ*, **139**, 1782
- Lantz B., et al., 2004, in Mazuray L., Rogers P. J., Wartmann R., eds, Proc. SPIE Vol. 5249, Optical Design and Engineering. pp 146–155, doi:10.1117/12.512493
- Law-Smith J., Ramirez-Ruiz E., Ellison S. L., Foley R. J., 2017, *ApJ*, **850**, 22
- Law-Smith J., Guillochon J., Ramirez-Ruiz E., 2019, *ApJ*, **882**, L25
- Leloudas G., et al., 2019, arXiv e-prints,
- Liu T., et al., 2017, *ApJS*, **232**, 8
- Liu X.-L., Dou L.-M., Shen R.-F., Chen J.-H., 2019, arXiv e-prints, p. arXiv:1912.06081
- Lodato G., Rossi E. M., 2011, *MNRAS*, **410**, 359
- Lodato G., King A. R., Pringle J. E., 2009, *MNRAS*, **392**, 332
- Lodato G., Franchini A., Bonnerot C., Rossi E. M., 2015, *Journal of High Energy Astrophysics*, **7**, 158
- Lu W., Bonnerot C., 2020, *MNRAS*, **492**, 686
- Lupton R., 2005, http://www.sdss.org/dr5/algorithms/sdssUBVRITransform.h
- MacLeod C. L., et al., 2012, *ApJ*, **753**, 106
- Magorrian J., et al., 1998, *AJ*, **115**, 2285
- Marchesi S., et al., 2016, *ApJ*, **830**, 100
- Martin D. C., et al., 2005, *ApJ*, **619**, L1
- McConnell N. J., Ma C.-P., 2013, *ApJ*, **764**, 184
- Mendel J. T., Simard L., Palmer M., Ellison S. L., Patton D. R., 2014, *ApJS*, **210**, 3
- Metzger B. D., Stone N. C., 2016, *MNRAS*, **461**, 948
- Miller J. M., et al., 2015, *Nature*, **526**, 542
- Mockler B., Guillochon J., Ramirez-Ruiz E., 2019, *ApJ*, **872**, 151
- Moretti A., et al., 2004, in Flanagan K. A., Siegmund O. H. W., eds, Proc. SPIE Vol. 5165, X-Ray and Gamma-Ray Instrumentation for Astronomy XIII. pp 232–240, doi:10.1117/12.504857
- Neustadt J. M. M., et al., 2019, arXiv e-prints, p. arXiv:1910.01142
- Nugent P. E., et al., 2011, *Nature*, **480**, 344
- Oke J. B., et al., 1995, *PASP*, **107**, 375
- Pasham D. R., et al., 2015, *ApJ*, **805**, 68
- Pasham D., Gendreau K., Arzoumanian Z., Kara E., 2019, The Astronomer's Telegram, 13221, 1
- Patterson M. T., et al., 2019, *PASP*, **131**, 018001
- Phinney E. S., 1989, *Nature*, **340**, 595
- Pogge R. W., et al., 2010, The multi-object double spectrographs for the Large Binocular Telescope. p. 77350A, doi:10.1117/12.857215
- Poole T. S., et al., 2008, *MNRAS*, **383**, 627
- Prieto J. L., Rest A., Suntzeff N. B., 2006, *ApJ*, **647**, 501
- Prieto J. L., et al., 2016, *ApJ*, **830**, L32

- Rees M. J., 1988, *Nature*, **333**, 523
- Ricci C., et al., 2017, *ApJS*, **233**, 17
- Rich J. A., Kewley L. J., Dopita M. A., 2015, *ApJS*, **221**, 28
- Richardson D., Jenkins Robert L. I., Wright J., Maddox L., 2014, *AJ*, **147**, 118
- Riess A. G., et al., 1999, *AJ*, **118**, 2675
- Roming P. W. A., et al., 2005, *SSR*, **120**, 95
- Roth N., Kasen D., Guillochon J., Ramirez-Ruiz E., 2016, *ApJ*, **827**, 3
- Ryu T., Krolik J., Piran T., Noble S. C., 2020, arXiv e-prints, p. [arXiv:2001.03501](#)
- Salpeter E. E., 1955, *ApJ*, **121**, 161
- Sarzi M., Rix H.-W., Shields J. C., Ho L. C., Barth A. J., Rudnick G., Filippenko A. V., Sargent W. L. W., 2005, *ApJ*, **628**, 169
- Saxton R. D., Read A. M., Esquej P., Freyberg M. J., Altieri B., Bermejo D., 2008, *A&A*, **480**, 611
- Schlaflly E. F., Finkbeiner D. P., 2011, *ApJ*, **737**, 103
- Schlegel D. J., Finkbeiner D. P., Davis M., 1998, *ApJ*, **500**, 525
- Shappee B. J., et al., 2014, *ApJ*, **788**, 48
- Shiokawa H., Krolik J. H., Cheng R. M., Piran T., Noble S. C., 2015, *ApJ*, **804**, 85
- Short P., et al., 2020, arXiv e-prints, p. [arXiv:2003.05470](#)
- Skrutskie M. F., et al., 2006, *AJ*, **131**, 1163
- Smith K. W., et al., 2019, *Research Notes of the American Astronomical Society*, **3**, 26
- Smith K. W., et al., 2020, arXiv e-prints, p. [arXiv:2003.09052](#)
- Stern D., et al., 2004, *ApJ*, **612**, 690
- Stone N. C., Kesden M., Cheng R. M., van Velzen S., 2019, *General Relativity and Gravitation*, **51**, 30
- Strubbe L. E., Murray N., 2015, *MNRAS*, **454**, 2321
- Svirski G., Piran T., Krolik J., 2017, *MNRAS*, **467**, 1426
- Tonry J. L., et al., 2018, *PASP*, **130**, 064505
- Tozzi P., et al., 2006, *A&A*, **451**, 457
- Ulmer A., 1999, *ApJ*, **514**, 180
- Veilleux S., Osterbrock D. E., 1987, *ApJS*, **63**, 295
- Vinkó J., et al., 2015, *ApJ*, **798**, 12
- Wang X.-Y., Liu R.-Y., 2016, *Phys. Rev. D*, **93**, 083005
- Wevers T., van Velzen S., Jonker P. G., Stone N. C., Hung T., Onori F., Gezari S., Blagorodnova N., 2017, *MNRAS*, **471**, 1694
- Wevers T., et al., 2019a, *MNRAS*, **487**, 4136
- Wevers T., et al., 2019b, *MNRAS*, **488**, 4816
- Wright E. L., et al., 2010, *AJ*, **140**, 1868
- York D. G., et al., 2000, *AJ*, **120**, 1579
- van Velzen S., 2018, *ApJ*, **852**, 72
- van Velzen S., Farrar G. R., 2014, *ApJ*, **792**, 53
- van Velzen S., et al., 2011, *ApJ*, **741**, 73
- van Velzen S., Gezari S., Hung T., Gatkine P., Cenko S. B., Ho A., Kulkarni S. R., Mahabal A., 2019, *The Astronomer's Telegram*, **12568**, 1
- van Velzen S., et al., 2020, arXiv e-prints, p. [arXiv:2001.01409](#)

This paper has been typeset from a \LaTeX file prepared by the author.

Table 6. Spectroscopic Observations of ASASSN-19dj

| MJD | Date | Telescope | Instrument | Rest Wavelength Range (Å) | Exposure Time (s) |
|---------|--------------------|-------------------------------------|------------|------------------------------|----------------------|
| 58539.2 | 2019 February 25.2 | ESO New Technology Telescope 3.58-m | EFOSC2 | 3555–9027 | 1×300 |
| 58546.1 | 2019 March 4.1 | du Pont 100-in | WFCCD | 3717–9390 | 1×900 |
| 58548.1 | 2019 March 6.1 | du Pont 100-in | WFCCD | 3717–9390 | 3×900 |
| 58550.1 | 2019 March 8.1 | du Pont 100-in | WFCCD | 3717–9390 | 1×900 |
| 58554.3 | 2019 March 12.3 | University of Hawaii 88-in | SNIFS | 3229–9489 | 3×1800 |
| 58572.0 | 2019 March 30.0 | Magellan Clay 6.5-m | LDSS-3 | 3619–9048 | 1×400 |
| 58573.3 | 2019 March 31.3 | Keck I 10-m | LRISp | 3130–9781 | 4×1800 |
| 58583.1 | 2019 April 10.1 | du Pont 100-in | WFCCD | 3717–9390 | 3×900 |
| 58612.3 | 2019 May 9.3 | University of Hawaii 88-in | SNIFS | 3229–9489 | 2×1800 |
| 58789.6 | 2019 November 2.6 | University of Hawaii 88-in | SNIFS | 3229–9489 | 2×2100 |
| 58806.3 | 2019 November 19.3 | Magellan Baade 6.5-m | IMACS | 4157–9195 | 4×900 |
| 58811.3 | 2019 November 24.3 | du Pont 100-in | WFCCD | 3717–9390 | 1×1200 |
| 58816.5 | 2019 November 29.5 | University of Hawaii 88-in | SNIFS | 3229–9489 | 1×3600 |
| 58839.3 | 2019 December 22.3 | Large Binocular Telescope 8.4 m | MODS | 3130–9781 | 4×1200 |

Modified Julian Day, calendar date, telescope, instrument, wavelength range, and exposure time for each of the spectroscopic observations obtained of ASASSN-19dj for the initial classification and during our follow-up campaign.